

Temperature dependence of photoluminescence intensity and spin contrast in nitrogen-vacancy centers

S. Ernst^{1,†}, P. J. Scheidegger^{1,†}, S. Diesch¹, L. Lorenzelli¹, and C. L. Degen^{1,2*}
¹*Department of Physics, ETH Zurich, Otto Stern Weg 1, 8093 Zurich, Switzerland. and*
²*Quantum Center, ETH Zurich, 8093 Zurich, Switzerland.*
(Dated: September 1, 2023)

We report on measurements of the photoluminescence (PL) properties of single nitrogen-vacancy (NV) centers in diamond at temperatures between 4–300 K. We observe a strong reduction of the PL intensity and spin contrast between ca. 10–100 K that recovers to high levels below and above. Further, we find a rich dependence on magnetic bias field and crystal strain. We develop a comprehensive model based on spin mixing and orbital hopping in the electronic excited state that quantitatively explains the observations. Beyond a more complete understanding of the excited-state dynamics, our work provides a novel approach for probing electron-phonon interactions and a predictive tool for optimizing experimental conditions for quantum applications.

The long coherence time [1] and the ease of optical spin readout have made the negatively charged nitrogen-vacancy (NV) center in diamond a preferred qubit for applications in quantum metrology [2] and quantum information [3]. Extraordinarily, the NV retains its quantum properties up to above room temperature, suggesting its use in both ambient and cryogenic environments. At room temperature, researchers have employed the NV's spin as a sensor for magnetic [4, 5] and electric fields [6], and thermometry [7, 8]. Cooled to below 10 K, spin-dependent optical transitions [9] have facilitated the implementation of prototypical quantum networks [10] and multi-qubit quantum operations [11]. Additionally, cryogenic NV magnetometry has been performed at the micron- [12] and nanoscale [13, 14].

While the photodynamics of NV centers at low temperature (below 10 K) and around room temperature have been studied in detail, the understanding in the intermediate temperature range is incomplete. Initial studies of the photoluminescence (PL) emission intensity of NV ensembles revealed a minimum around 25 K attributed to time-averaging in the electronic excited state (ES) [15]. This averaging process is caused by phonon-mediated transitions between the two orbital branches [16, 17]. A temperature-dependent reduction in PL intensity and spin contrast was also reported in connection with NV charge state instabilities [18]. Further, spin mixing in the ES due to magnetic field [19, 20] or crystal strain [21] was identified as another mechanism for loss of PL. The strain-related spin mixing at low temperature was found to be partially mitigated by application of a large magnetic bias field [15, 20, 22]. Because high PL intensity and spin contrast are essential for high-fidelity quantum readout and sensitive magnetometry, a complete picture of the NV photodynamics in the 10–100 K range is highly desirable.

In this Letter, we report measurements of the PL intensity and spin contrast for single NV centers between 4–300 K. We show that a combination of orbital hopping and spin mixing in the ES leads to a strong reduction of

both quantities between 10 – 100 K. Based on measurements at varying magnetic field (0 – 200 mT) and intrinsic strain (ES splitting $2 \times (9 - 80)$ GHz), we develop a comprehensive theoretical model for the temperature-dependent dynamics of the ES. Details on the model and simulation framework are given in a companion paper [23]. As a result, we are able to quantitatively describe the NV's PL intensity and spin contrast over the complete parameter range of temperature, magnetic field and strain, and find excellent agreement with experimental data.

In our study, we investigate single NV centers situated in nanostructured pillars, which serve to enhance the photon collection efficiency. Our samples include an array of pillars on isotopically pure ^{12}C diamond (NV-1 to NV-4, ElementSix) and a scanning tip fabricated from natural-abundance material (NV-5, QZabre). NV centers are formed by shallow $^{15}\text{N}^+$ ion implantation (7 keV) followed by high-temperature annealing ($< 10^{-8}$ mbar, 880 °C, 2 h). Samples are measured in a dry dilution refrigerator (Setup A) at temperatures between 4 – 100 K; an additional study down to 0.35 K did not show further variation in the NV behavior [24]. A second dry cryostat (Setup B) with a temperature range of 30 – 300 K is used to validate the aforementioned measurements and extend the range to room temperature [25]. Both setups operate in vacuum without addition of exchange gas ($p < 5.5 \cdot 10^{-5}$ mbar). Magnetic bias fields, when specified, are applied along the NV symmetry axis.

The central experimental observation of this work is reported in Fig. 1, which plots the spin contrast as a function of temperature $T = 4 - 300$ K. The PL intensity follows a similar trend (see Fig. S7), but is more prone to experimental drift. We measure the contrast by integrating the relative difference in PL between the $m_S = 0$ and $m_S = -1$ states (subsequently denoted by $|0\rangle$ and $|-1\rangle$) during the first 250 ns under excitation with a 520 nm diode laser (Fig. 1(a)). To initialize the spin state into $|0\rangle$, we use a $2 \mu\text{s}$ laser pulse, followed by a state swap to $|-1\rangle$ (when needed) using an adiabatic in-

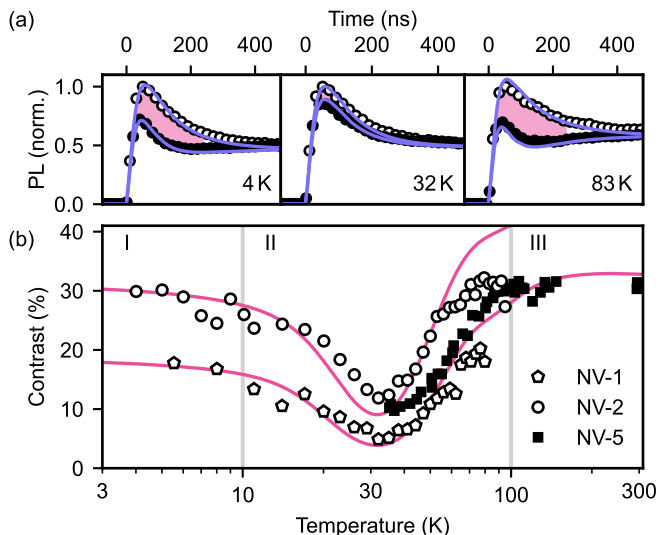


Figure 1. (a) Time-dependent PL traces during a laser pulse, measured on NV-2 initialized to the $|0\rangle$ (open circles) and $|-1\rangle$ (filled circles) states at low, intermediate and high temperature. The spin contrast is given by the relative difference between the two curves (pink shading). Solid lines are fits to the PL dynamics. (b) Spin contrast versus temperature for three NV centers measured on Setup A (empty markers) and Setup B (filled marker). Solid lines show corresponding simulations for NV-1 and NV-2. A bias field of 3 mT is applied.

version microwave pulse [26]. Fig. 1(b) clearly reveals three temperature regimes: (I) Below ca. 10 K, the spin contrast is mostly constant. (II) Between ca. 10 – 100 K, the spin contrast is strongly reduced with a pronounced minimum around 35 K and then recovers for higher temperatures. (III) Above ca. 100 K, the spin contrast remains approximately constant up to room temperature. In all measurements, the room temperature contrast exceeds the low temperature limit. At even higher temperatures, the contrast has been shown to slowly decrease until it vanishes around 700 K [27].

Before providing a theoretical explanation for the behavior seen in Fig. 1, we briefly recall the mechanism for contrast generation by looking at the spin-subspace of the NV given in Fig 2(a) [28]. After spin-conserving optical excitation from the ground state (GS) into the ES, a spin-selective intersystem crossing (ISC) leads to preferential population of the shelving state for $|\pm 1\rangle$. Because the shelving state 1E has a relatively long lifetime, the average PL emission is lower for $|\pm 1\rangle$ compared to $|0\rangle$, leading to spin contrast. The PL reduction is temporary and disappears due to optical re-pumping into $|0\rangle$ after a few hundred nanoseconds, see Fig 1(a). Crucially, this mechanism of contrast generation is effective only for as long as there are no transitions between the ES spin states.

We next consider the orbital subspace of the NV ES (3E), which is a doublet shown in Fig. 2(b) [28]. In the

presence of in-plane strain δ_{\perp} relative to the NV principal axis, the ES possesses two orbital branches, E_x and E_y , split by $2\delta_{\perp}$ [29]. In the composite space of orbit and spin, each branch has three spin states, leading to a total of six energy eigenlevels (Fig. 2(c)). We now show that the contrast reduction and recovery can be explained by the interplay of two mechanisms: spin mixing and orbital branch hopping in the ES.

First, we discuss the effects of spin mixing, meaning that the ES eigenstates are not pure spin eigenstates. As an example, we consider Fig. 2(c). Here, the $|0\rangle$ state is in good approximation an eigenstate of the E_x branch but not the E_y branch, where it forms a superposition with the $|-\rangle \propto (|+1\rangle - |-1\rangle)$ state. Consequently, optical excitation into the E_x branch is spin-conserving, while excitation into the E_y branch will lead to spin mixing. In general, the spin mixing amplitudes $\epsilon_{|i\rangle,|j\rangle}$ between basis states $|i\rangle$ and $|j\rangle$ in the six eigenlevels depend on the strain magnitude and direction [21, 30], as well as magnetic field alignment [19] and magnitude [20]. Therefore, the spin contrast is both strain and field-dependent. Although the $\epsilon_{|i\rangle,|j\rangle}$ are typically small, they play a key role in the mechanism of spin relaxation.

Second, we consider the effects of orbital hopping, which refers to spin-conserving transitions between E_x and E_y driven by phonons. Fig. 2(b) schematically depicts the dominant contributions arising from one-phonon processes (rates k_1) and two-phonon processes (rates k_2) derived in Ref. [23, 31, 32]. The one-phonon downward ($E_x \rightarrow E_y$) hopping rate is given by

$$k_{\downarrow,1}(T, \delta_{\perp}) \propto \eta \delta_{\perp}^3 [n(2h\delta_{\perp}/k_B T) + 1], \quad (1)$$

where η parametrizes the electron-phonon coupling and n is the Bose-Einstein distribution function. The rate of the two-phonon process is given by

$$k_{\downarrow,2}(T) \propto \eta^2 T^5 I(T). \quad (2)$$

where $I(T)$ is a mildly strain- and temperature-dependent integral over the phonon spectrum that we solve in the Debye approximation. The total hopping rates are the sums of the one- and two-phonon contributions, $k_{\downarrow(\uparrow)} = k_{\downarrow(\uparrow),1} + k_{\downarrow(\uparrow),2}$. The upward ($E_y \rightarrow E_x$) rate significantly differs from the downward rate only below 10 K, where it is reduced by the absence of spontaneous emission (second term in Eq. 1). Fig. 2(d) plots the hopping rates for the parameters in Fig. 2(c) as a function of temperature. It provides the key to explaining our experimental observations in the temperature regimes (I-III):

(I) Below ca. 10 K, the orbital hopping is dominated by $k_{\downarrow,1}$ due to the spontaneous emission. Since $k_{\downarrow,1}$ is slower than the ES decay rate ($T_{3E}^{-1} \approx 10^8 \text{ s}^{-1}$) for typical strain values $\delta_{\perp} \lesssim 40 \text{ GHz}$, the ES spin states are mostly preserved (except for some small spin mixing ϵ_i) and the spin contrast is high.

(II) Above 10 K, the two-phonon process starts to dominate. Once $k > T_{3E}^{-1}$, spin relaxation between $|0\rangle$ and $|\pm 1\rangle$ is drastically amplified, because the time evolution under different Larmor precession in both branches becomes randomized by the frequent hopping. This relaxation mechanism is most efficient when a hopping event occurs approximately every half of a Larmor precession period $(2\omega_{x(y)})^{-1}$ [23]. This occurs between ca. 30–40 K (gray shading in Fig. 2(d)) and coincides with the temperature where we observe the strongest suppression of the spin contrast.

(III) As the temperature increases further, the orbital hopping rates become much faster than the spin dynamics and the two orbital states are time-averaged [15, 29]. This effectively renders 3E an orbital singlet similar to the GS 3A_2 [33] and leads to the commonly accepted room-temperature model appearing as in Fig. 2(a). Since $|0\rangle$ and $|\pm 1\rangle$ are pure eigenstates of the time-averaged Hamiltonian, the highest spin contrast is observed in this regime.

Armed with this theory, we implement a rate model to quantitatively reproduce the experimental observations by numerical simulations. Details on the rate model and simulations are given in a companion paper [23] and the Supplemental Information. We model the orbital hopping by spin-conserving Markovian transitions between the two orbital branches. Since spin coherences are maintained during the transitions, we use a Lindblad master equation rather than a classical rate model. We describe the ES in a composite Hilbert space of spin and orbit ($\mathcal{H}_{ES} = \mathcal{H}_{orbit} \otimes \mathcal{H}_{spin}$) and formulate the spin-conserving jump operators as

$$L_{\downarrow}^{ES} = \sqrt{k_{\downarrow,1} + k_{\downarrow,2}} |y\rangle\langle x| \otimes \mathbb{I}_3, \quad (3)$$

and likewise for L_{\uparrow}^{ES} . We further introduce optical excitation, decay and ISC by classical jump operators. The resulting Liouville equation describes the time evolution of the 10-dimensional density matrix $\rho(t)$, containing three GS levels, six ES levels and one combined shelving state.

To simulate the behavior of a chosen NV center, we feed our model with values obtained from a simultaneous fit of three sets of calibration measurements: (i) We use a measurement of the steady-state PL intensity as a function of magnetic field at base temperature (see Fig. 3(b, 4 K)) to obtain strain values and unintended misalignment of the bias field, fitting the minima in the PL at level anti-crossings [15, 20]. (ii) We pick a set of 24 time-dependent PL traces (c.f. Fig. 1(a)), including two spin states ($|0\rangle$, $|-1\rangle$), six temperatures (4–100 K), and low and high bias field (3 mT, 200 mT). Fits to these PL traces then yield the optical decay and ISC rates, which are approximately temperature-independent [34] and are known to vary between NV centers [28, 35], as well as the coupling strength η . We determine the shelving state lifetime [30, 35], which has a mild, well-known temperature dependence, in a separate calibration. (iii) For each

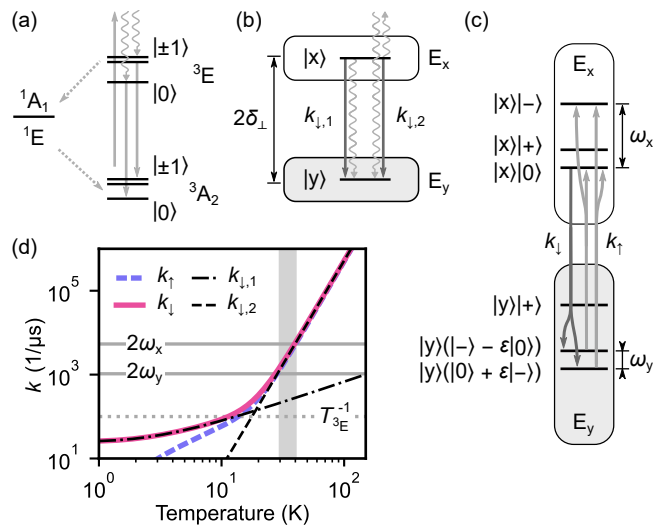


Figure 2. (a) Level diagram in the NV spin subspace \mathcal{H}_{spin} of the electronic ground (3A_2) and excited (3E) states, as well as the metastable (1A_1 , 1E) shelving states. The intersystem crossing (dotted) is spin selective, favoring decay out of $|\pm 1\rangle$. In (a-c), solid arrows mark spin-conserving transitions and curly arrows symbolize phonons. (b) Level diagram in the orbital subspace \mathcal{H}_{orbit} of the NV ES (3E). Two orbital branches (E_x , E_y) split under strain δ_{\perp} . One- and two-phonon processes cause hopping between branches at temperature-dependent rates $k_{\downarrow,1(2)}$ ($k_{\uparrow,1(2)}$ not shown). (c) Example of levels in the composite Hilbert space of orbit and spin $\mathcal{H}_{orbit} \otimes \mathcal{H}_{spin}$. Eigenstates are superpositions of $|0\rangle$ and $|\pm\rangle \propto (|+1\rangle \pm |-1\rangle)$. Spin-conserving, phonon-mediated transitions involving $|0\rangle$ are depicted by gray arrows. $\omega_{x(y)}$ are the Larmor frequencies of involved spin transitions. (d) Hopping rates as a function of temperature. Inverse optical lifetime T_{3E}^{-1} and Larmor frequencies (in MHz) are indicated by horizontal lines. For (c, d) we use $\delta_{\perp} = 40$ GHz in the direction of a carbon bond at low magnetic field, such that only two basis states mix significantly ($|\varepsilon|^2 = |\varepsilon_{|y,0\rangle,|y,-\rangle}|^2 = 0.1$ in Tab. III).

time-dependent PL trace, we perform an optical saturation measurement to quantify drift in the background luminescence, optical alignment, and ratio of collection over excitation efficiency. Finally, we use literature values for the NV fine structure [36, 37].

As an important side result, our calibration yields values for the electron-phonon couplings η ranging from $176 \mu s^{-1} meV^{-3}$ (NV-2, used in Fig. 2(d)) to $268 \mu s^{-1} meV^{-3}$ (NV-4), in good agreement with Refs. [17, 31, 32]. We note that these studies use different phonon models in the evaluation of $I(T)$. While our data does not allow validation of a particular model with certainty, our measurement approach provides complementary insight into $I(T)$ [23] (see also Fig. S6).

We are now ready to return to Fig. 1(b) and use our model and calibration to simulate the temperature-dependent PL and spin contrast (solid curves). Overall, we find an excellent agreement between experimental and

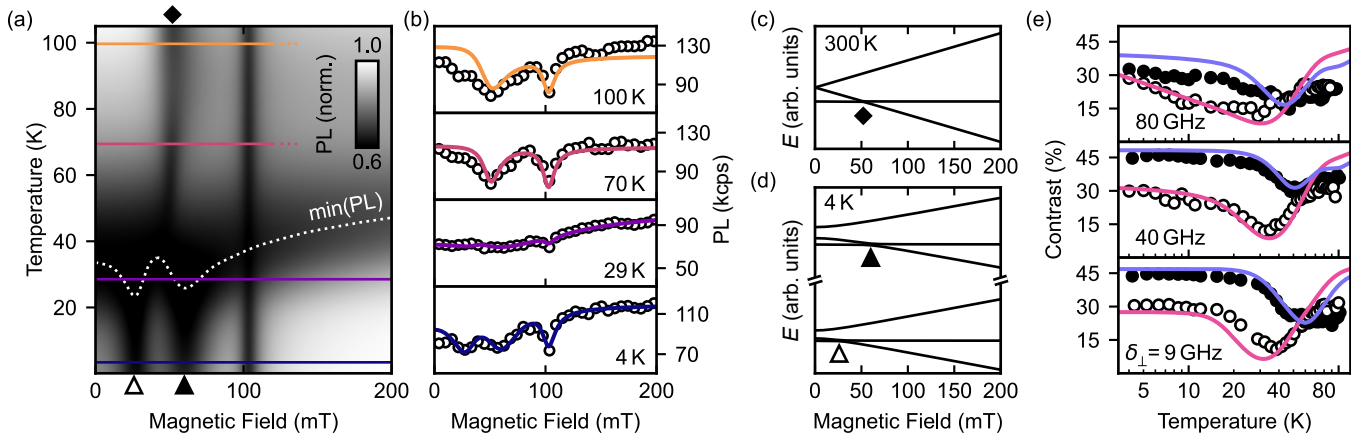


Figure 3. (a) Simulation of the PL in dependence of the magnetic field and temperature. The PL is strongly reduced at avoided crossings of the excited state (symbols) and the ground state (103 mT) energy levels. The white dotted line marks the PL minimum, coloured solid lines indicate the line cuts shown in (b). The simulation is based on parameters fitted to NV-1. (b) Experimental PL curves for NV-1 measured as a function of magnetic field and temperature. Solid lines are fits. (c,d) Energy levels for the NV-1 ES at 300 K (c, time-averaged) and at 4 K (d). Symbols refer to (a). (e) Experimental spin contrast as a function of temperature for NV centers with different strain δ_{\perp} . Measurements are taken at 3 mT (empty circles) and 200 mT (filled circles). Solid lines show the corresponding simulations.

simulated results. In particular, the model quantitatively reproduces all temperature regimes (I-III), including the minimum in contrast around 35 K and the recovery towards room temperature. Although the agreement is not perfect at elevated temperatures, which we attribute to setup instabilities and uncertainty in temperature calibration (see Supplemental Information I), our model successfully bridges the classical rate models used in the limits of low [20] and high [19, 35] temperatures.

Next, we use our model to predict the PL properties as a function of magnetic bias field. In Fig. 3(a,b), we plot the simulated PL intensity as a function of $B = 0 - 200$ mT and $T = 0 - 100$ K together with the experimental results. The model successfully predicts the known reductions in PL (indicated by symbols) at magnetic fields that correspond to level-anti-crossings (LAC) in the ES, in both the low (Fig. 3(d)) and high temperature limit (Fig. 3(c), obtained from Fig. 3(d) by a partial trace over the orbital subspace). The global PL minimum – indicated by the dotted line in Fig. 3(a) – depends on the exact energy level spacing at a given magnetic field (and strain). For example, we observe that with increasing magnetic field (beyond the second ES LAC), the PL minimum becomes less pronounced and shifts to higher temperatures. This behavior is readily explained by a lower degree of spin mixing in the eigenstates (smaller $\epsilon_{|i\rangle,|j\rangle}$ in Fig. 2(c)) and higher Larmor frequencies (larger $\omega_{x(y)}$ in Fig. 2(d)) at high field. However, even at the highest field accessible in our experiment (200 mT), the PL minimum is still noticeable. Full recovery of the PL is expected for fields significantly above 1 T (Fig. S10).

Finally, we examine the influence of crystal strain. In Fig. 3(e), we compare the temperature dependence of the

spin contrast for NV centers with high (NV-4, 80 GHz), medium (NV-2, 40 GHz), and low (NV-3, 9 GHz) intrinsic strain within our accessible range (NV-1 has 32 GHz). While all curves show the same qualitative behavior, we find that the most prominent feature is a decrease in the spin contrast at high strain δ_{\perp} already below 10 K. This feature can be understood through the factor δ_{\perp}^3 in Eq. 1: $k_{\uparrow,1}$ is rapidly increasing as the required high energy phonon modes become thermally activated, approaching $k_{\downarrow,1}$, which is generally high due to spontaneous emission (Fig. S11).

In conclusion, we developed a rate model that explains the NV center photo-physics over a broad range of temperature, magnetic bias field and crystal strain, and find excellent agreement with the experiment. In particular, our model successfully predicts a minimum in the PL emission and spin contrast around 35 K due to rapid spin relaxation driven by an interplay of spin mixing and orbital hopping. This spin relaxation process degrades both the spin initialization and the spin readout fidelity (Fig. S9). It is of fundamental nature and universal to all NV centers, including NV centers deep in the bulk that experience negligible crystal strain [29] (Fig. S10).

Our work provides useful insight beyond giving a more complete picture of the NV excited-state dynamics. Firstly, our model can account for the observed temperature dependence by phonon-induced processes in the ES alone. Therefore, we conclude that charge-state switching between NV^{-} and NV^0 does not play a key role in explaining the spin contrast as a function of temperature. We also have not observed any signs of charge state instabilities on the few-minutes time scale of our measurements (see Fig. S2). Second, our work intro-

duces a new measurement approach for probing electron-phonon interactions and contributing modes, applicable in regimes where resonant laser PL excitation spectroscopy [31] or measurement of motional narrowing on ES ODMR lines [32] are unavailable. Third, we examined the rich dependence on magnetic field, strain (or equivalently electric field [28]), and temperature. Here, our model offers a predictive tool for maximizing the PL intensity and spin contrast, which are the key quantities for achieving high spin readout fidelity and high metrology sensitivity in quantum applications.

Note added: We acknowledge related work on the temperature dependence of the NV photo-physics by Happacher *et al.* [38] and Blakley *et al.* [39].

The authors thank Matthew Markham (ElementSix) for providing the ^{12}C diamond, Jan Rhensius (QZabre) for nanofabrication, and Erika Janitz, Fedor Jelezko, Assaf Hamo, Konstantin Herb, William Huxter, Patrick Maletinsky, Francesco Poggiali, Friedemann Reinhard, Jörg Wrachtrup and Jonathan Zopes for useful input and discussions. This work was supported by the European Research Council through ERC CoG 817720 (IMAGINE), the Swiss National Science Foundation (SNSF) through Project Grant No. 200020_175600 and through the NCCR QSIT, a National Centre of Competence in Research in Quantum Science and Technology, Grant No. 51NF40-185902, and the Advancing Science and TEchnology thRough dIamond Quantum Sensing (ASTERIQS) program, Grant No. 820394, of the European Commission.

* degenc@ethz.ch; †These authors contributed equally.

- [1] E. D. Herbschleb, H. Kato, Y. Maruyama, T. Danjo, T. Makino, S. Yamasaki, I. Ohki, K. Hayashi, H. Morishita, M. Fujiwara, and N. Mizuochi, Ultra-long coherence times amongst room-temperature solid-state spins, *Nat. Commun.* **10**, 3766 (2019).
- [2] R. Schirhagl, K. Chang, M. Loretz, and C. L. Degen, Nitrogen-vacancy centers in diamond: Nanoscale sensors for physics and biology, *Annu. Rev. Phys. Chem.* **65**, 83 (2014).
- [3] L. Childress and R. Hanson, Diamond NV centers for quantum computing and quantum networks, *MRS Bulletin* **38**, 134 (2013).
- [4] J. R. Maze, P. L. Stanwix, J. S. Hodges, S. Hong, J. M. Taylor, P. Cappellaro, L. Jiang, M. V. G. Dutt, E. Togan, A. S. Zibrov, A. Yacoby, R. L. Walsworth, and M. D. Lukin, Nanoscale magnetic sensing with an individual electronic spin in diamond, *Nature* **455**, 644 (2008).
- [5] G. Balasubramanian, I. Y. Chan, R. Kolesov, M. Al-Hmoud, J. Tisler, C. Shin, C. Kim, A. Wojcik, P. R. Hemmer, A. Krueger, T. Hanke, A. Leitenstorfer, R. Bratschkitsch, F. Jelezko, and J. Wrachtrup, Nanoscale imaging magnetometry with diamond spins under ambient conditions, *Nature* **455**, 648 (2008).
- [6] F. Dolde, H. Fedder, M. W. Doherty, T. Noebauer, F. Rempp, G. Balasubramanian, T. Wolf, F. Reinhard, L. C. L. Hollenberg, F. Jelezko, and J. Wrachtrup, Electric-field sensing using single diamond spins, *Nat. Phys.* **7**, 459 (2011).
- [7] G. Kucsko, P. C. Maurer, N. Y. Yao, M. Kubo, H. J. Noh, P. K. Lo, H. Park, and M. D. Lukin, Nanometre-scale thermometry in a living cell, *Nature* **500**, 54 (2013).
- [8] V. M. Acosta, E. Bauch, M. P. Ledbetter, A. Waxman, L. S. Bouchard, and D. Budker, Temperature dependence of the nitrogen-vacancy magnetic resonance in diamond, *Phys. Rev. Lett.* **104**, 070801 (2010).
- [9] L. Robledo, L. Childress, H. Bernien, B. Hensen, P. F. A. Alkemade, and R. Hanson, High-fidelity projective readout of a solid-state spin quantum register, *Nature* **477**, 574 (2011).
- [10] M. Pompili, S. L. N. Hermans, S. Baier, H. K. C. Beukers, P. C. Humphreys, R. N. Schouten, R. F. L. Vermeulen, M. J. Tiggelman, L. dos Santos Martins, B. Dirkse, S. Wehner, and R. Hanson, Realization of a multinode quantum network of remote solid-state qubits, *Science* **372**, 259 (2021).
- [11] C. Bradley, J. Randall, M. Abobeih, R. Berrevoets, M. Degen, M. Bakker, M. Markham, D. Twitchen, and T. Taminiau, A ten-qubit solid-state spin register with quantum memory up to one minute, *Phys. Rev. X* **9**, 031045 (2019).
- [12] S. E. Lillie, D. A. Broadway, N. Dontschuk, S. C. Scholten, B. C. Johnson, S. Wolf, S. Rachel, L. C. L. Hollenberg, and J.-P. Tetienne, Laser modulation of superconductivity in a cryogenic wide-field nitrogen-vacancy microscope, *Nano Lett.* **20**, 1855 (2020).
- [13] T. Song, Q. C. Sun, E. Anderson, C. Wang, J. Qian, T. Taniguchi, K. Watanabe, M. A. McGuire, R. Stohr, D. Xiao, T. Cao, J. Wrachtrup, and X. Xu, Direct visualization of magnetic domains and Moire magnetism in twisted 2D magnets, *Science* **374**, 1140 (2021).
- [14] L. Thiel, Z. Wang, M. A. Tschudin, D. Rohner, I. Gutierrez-lezama, N. Ubrig, M. Gibertini, E. Gianini, A. F. Morpurgo, and P. Maletinsky, Probing magnetism in 2D materials at the nanoscale with single-spin microscopy, *Science* **364**, 973 (2019).
- [15] L. J. Rogers, R. L. McMurtrie, M. J. Sellars, and N. B. Manson, Time-averaging within the excited state of the nitrogen-vacancy centre in diamond, *New J. Phys.* **11**, 063007 (2009).
- [16] K. C. Fu, C. Santori, P. E. Barclay, L. J. Rogers, N. B. Manson, and R. G. Beausoleil, Observation of the dynamic Jahn-Teller effect in the excited states of nitrogen-vacancy centers in diamond, *Phys. Rev. Lett.* **103**, 256404 (2009).
- [17] T. A. Abtew, Y. Y. Sun, B. Shih, P. Dev, S. B. Zhang, and P. Zhang, Dynamic Jahn-Teller effect in the NV⁻ center in diamond, *Phys. Rev. Lett.* **107**, 146403 (2011).
- [18] D. F. Wise, *Could NV centres in diamond be used to measure donor spins in silicon?*, *PhD Thesis*, University College London, London (2021).
- [19] J. Tetienne, L. Rondin, P. Spinicelli, M. Chipaux, T. Debuisschert, J. Roch, and V. Jacques, Magnetic-field-dependent photodynamics of single NV defects in diamond: an application to qualitative all-optical magnetic imaging, *New J. Phys.* **14**, 103033 (2012).
- [20] J. Happacher, D. A. Broadway, J. Bocquel, P. Reiser, A. Jimenez, M. A. Tschudin, L. Thiel, D. Rohner, M. I. G. Puigibert, B. Shields, J. R. Maze, V. Jacques,

- and P. Maletinsky, Low-temperature photophysics of single nitrogen-vacancy centers in diamond, *Phys. Rev. Lett.* **128**, 177401 (2022).
- [21] P. Tamarat, N. B. Manson, J. P. Harrison, R. L. McMurtrie, A. Nizovtsev, C. Santori, R. G. Beausoleil, P. Neumann, T. Gaebel, F. Jelezko, P. Hemmer, and J. Wrachtrup, Spin-flip and spin-conserving optical transitions of the nitrogen-vacancy centre in diamond, *New J. Phys.* **10**, 045004 (2008).
- [22] U. Vool, A. Hamo, G. Varnavides, Y. Wang, T. X. Zhou, N. Kumar, Y. Dovzhenko, Z. Qiu, C. A. C. Garcia, A. T. Pierce, J. Gooth, P. Anikeeva, C. Felser, P. Narang, and A. Yacoby, Imaging phonon-mediated hydrodynamic flow in WTe₂, *Nat. Phys.* **17**, 1216 (2021).
- [23] S. Ernst, P. J. Scheidegger, S. Diesch, and C. L. Degen, Modeling temperature-dependent population dynamics in the excited state of the nitrogen-vacancy center in diamond, *Phys. Rev. B* **108**, 085203 (2023).
- [24] P. J. Scheidegger, S. Diesch, M. L. Palm, and C. L. Degen, Scanning nitrogen-vacancy magnetometry down to 350 mK, *Appl. Phys. Lett.* **120**, 224001 (2022).
- [25] L. Lorenzelli, *Development of a scanning nitrogen-vacancy-center magnetometer for variable temperature experiments*, PhD Thesis, ETH Zurich, Zurich (2021).
- [26] E. Kupce and R. Freeman, Adiabatic pulses for wideband inversion and broadband decoupling, *Journal of Magnetic Resonance, Series A* **115**, 273 (1995).
- [27] D. M. Toyli, D. J. Christle, A. Alkauskas, B. B. Buckley, C. G. van de Walle, and D. D. Awschalom, Measurement and control of single nitrogen-vacancy center spins above 600K, *Phys. Rev. X* **2**, 031001 (2012).
- [28] M. W. Doherty, N. B. Manson, P. Delaney, F. Jelezko, J. Wrachtrup, and L. C. Hollenberg, The nitrogen-vacancy colour centre in diamond, *Phys. Rep.* **528**, 1 (2013).
- [29] A. Batalov, V. Jacques, F. Kaiser, P. Siyushev, P. Neumann, L. J. Rogers, R. L. McMurtrie, N. B. Manson, F. Jelezko, and J. Wrachtrup, Low temperature studies of the excited-state structure of negatively charged nitrogen-vacancy color centers in diamond, *Phys. Rev. Lett.* **102**, 195506 (2009).
- [30] N. Manson, J. Harrison, and M. Sellars, Nitrogen-vacancy center in diamond: model of the electronic structure, *Phys. Rev. B* **74**, 104303 (2006).
- [31] M. L. Goldman, A. Sipahigil, M. W. Doherty, N. Y. Yao, S. D. Bennett, M. Markham, D. J. Twitchen, N. B. Manson, A. Kubanek, and M. D. Lukin, Phonon-induced population dynamics and intersystem crossing in nitrogen-vacancy centers, *Phys. Rev. Lett.* **114**, 145502 (2015).
- [32] T. Plakhotnik, M. W. Doherty, and N. B. Manson, Electron-phonon processes of the nitrogen-vacancy center in diamond, *Phys. Rev. B* **92**, 081203 (2015).
- [33] T. Plakhotnik, M. W. Doherty, J. H. Cole, R. Chapman, and N. B. Manson, All-optical thermometry and thermal properties of the optically detected spin resonances of the NV⁻ center in nanodiamond, *Nano Lett.* **14**, 4989 (2014).
- [34] M. L. Goldman, M. W. Doherty, A. Sipahigil, N. Y. Yao, S. D. Bennett, N. B. Manson, A. Kubanek, and M. D. Lukin, State-selective intersystem crossing in nitrogen-vacancy centers, *Phys. Rev. B* **91**, 165201 (2015).
- [35] L. Robledo, H. Bernien, T. van der Sar, and R. Hanson, Spin dynamics in the optical cycle of single nitrogen-vacancy centres in diamond, *New J. Phys.* **13**, 025013 (2011).
- [36] L. C. Bassett, F. J. Heremans, D. J. Christle, C. G. Yale, G. Burkard, B. B. Buckley, and D. D. Awschalom, Ultrafast optical control of orbital and spin dynamics in a solid-state defect, *Science* **345**, 1333 (2014).
- [37] X. D. Chen, C. H. Dong, F. W. Sun, C. L. Zou, J. M. Cui, Z. F. Han, and G. C. Guo, Temperature dependent energy level shifts of nitrogen-vacancy centers in diamond, *Appl. Phys. Lett.* **99**, 161903 (2011).
- [38] J. Happacher, J. Bocquel, H. T. Dinani, M. A. Tschudin, P. Reiser, D. A. Broadway, J. R. Maze, and P. Maletinsky, Temperature dependent photophysics of single NV centers in diamond, *Phys. Rev. Lett.* **131**, 086904 (2023).
- [39] S. M. Blakley, T. T. Mai, S. J. Moxim, J. T. Ryan, A. J. Biacchi, A. R. H. Walker, and R. D. McMichael, Spectroscopy of photoionization from the ¹E singlet state in nitrogen-vacancy centers in diamond, [arXiv:2301.10383](https://arxiv.org/abs/2301.10383) (2023).
- [40] R. Ulbricht, S. Dong, I. Chang, B. M. K. Mariserla, K. M. Dani, K. Hyeon-Deuk, and Z. Loh, Jahn-teller-induced femtosecond electronic depolarization dynamics of the nitrogen-vacancy defect in diamond, *Nat. Commun.* **7**, 13510 (2016).
- [41] D. Wirtitsch, G. Wachter, S. Reisenbauer, M. Gulka, V. Ivády, F. Jelezko, A. Gali, M. Nesladek, and M. Trupke, Exploiting ionization dynamics in the nitrogen vacancy center for rapid, high-contrast spin, and charge state initialization, *Phys. Rev. Research* **5**, 013014 (2023).
- [42] M. L. Goldman, M. W. Doherty, A. Sipahigil, N. Y. Yao, S. D. Bennett, N. B. Manson, A. Kubanek, and M. D. Lukin, Erratum: State-selective intersystem crossing in nitrogen-vacancy centers [phys. rev. b 91, 165201 (2015)], *Phys. Rev. B* **96**, 039905 (2017).
- [43] A. Gali, Ab initio theory of the nitrogen-vacancy center in diamond, *Nanophotonics* **8**, 1907 (2019).
- [44] A. Dreau, M. Lesik, L. Rondin, P. Spinicelli, O. Arcizet, J. F. Roch, and V. Jacques, Avoiding power broadening in optically detected magnetic resonance of single NV defects for enhanced dc magnetic field sensitivity, *Phys. Rev. B* **84**, 195204 (2011).
- [45] D. A. Hopper, H. J. Shulevitz, and L. C. Bassett, Spin readout techniques of the nitrogen-vacancy center in diamond, *Micromachines* **9**, 437 (2018).
- [46] A. Gupta, L. Hacquebard, and L. Childress, Efficient signal processing for time-resolved fluorescence detection of nitrogen-vacancy spins in diamond, *J. Opt. Soc. Am. B* **33**, B28 (2016).
- [47] N. Kalb, P. C. Humphreys, J. J. Slim, and R. Hanson, Dephasing mechanisms of diamond-based nuclear-spin memories for quantum networks, *Phys. Rev. A* **97**, 062330 (2018).

Supplemental Material

CONTENTS

References	5
I. Experimental	8
II. Measurements	8
A. PL vs. B	8
B. Time-resolved pulsed ODMR	9
C. Saturation measurement	9
D. Shelving state lifetime	9
E. Continuous time tagging	10
III. The numerical model	10
A. Level structure and optical transition rates	10
B. Orbital hopping rates	11
C. Master equation	13
D. Linking simulation with experiment	13
E. Evaluating sensing performance	13
IV. Data fitting and simulation	14
A. Calibration	15
B. Calibration results	15
C. Simulations and fits	16
D. Influence of the phonon model on our simulation	17
V. Additional simulations	19
A. Contrast, PL and sensitivity	19
B. Optimal integration time	19
C. Spin initialization and readout fidelity	20
D. Extrapolation to low strain or high magnetic field	20
VI. Spin mixing amplitudes	21
VII. Strain dependence of orbital hopping rates	22

I. EXPERIMENTAL

The majority of data presented in this work was acquired inside a dilution refrigerator (Setup A) on an isotopically pure (^{12}C) diamond sample doped with 7keV NV centers in nanostructured pillars. To minimize heating by the microwave excitation, we employ an impedance-matched co-planar waveguide (CPW) made from thin-film aluminum on top of a sapphire substrate, which is identical to the CPW we used in our recent sub-Kelvin scanning magnetometry experiments [24]. To ensure good thermalization, we glue the diamond sample directly on top of the CPW, which in turn is glued on a sample holder made from copper. The sample holder contains both, a resistive heater and a calibrated thermometer (LakeShore Cernox). A PID controller is used to stabilize the temperature in a range from 4 K to 100 K with a temperature stability of 0.1K at low temperatures and $< 1\text{K}$ at very high temperatures. Towards higher measurement temperatures ($> 60\text{K}$), we increasingly find thermal drifts, which we stabilize by frequent optical tracking. Despite our efforts, one can observe that the contrast values measured in the high temperature limit are systematically lower than the simulated model (Fig. 1(b) and Fig. 3(e) of the main text). We attribute this to increased setup instabilities and possibly some uncertainty in the measured temperature, due to the large temperature gradient between the sample and the rest of the cryostat (Setup A).

For the optical excitation of the NV, we use a 520 nm diode-laser with home-built modulation circuitry. We characterize its rise time on fluorescent contamination in proximity to the NV center and obtain $\tau_R = 23 \pm 1\text{ ns}$. We calibrate the laser power directly at its output and use a conversion factor to fit the actual (lower) laser power on the NV. Heating of the diode slightly alters the output laser power, which is why we find a consistent mismatch by a factor of 1.15 between the steady-state PL value in *time-resolved pulsed ODMR* and the *saturation* measurements (for details, see section II) and we scale our data accordingly.

We use a superconducting vector magnet (American Magnetics Inc.) to apply a magnetic field along the respective NV axis. The field is aligned by sweeping both spherical angles at a constant field magnitude of $B = 200\text{ mT}$ and minimizing the ODMR resonance of the $m_S = -1$ state. This calibration has been performed once for every NV. As common for superconducting magnets, we observe a remanent field of approximately 3 mT (projected onto the NV axis) after operation at elevated magnetic fields (here: 200 mT). We can reset the magnet by heating it to above the superconducting transition temperature and letting it cool down again. In our experiments, we perform such a reset when switching to a different NV (i.e. moving the magnetic field orientation) and when lowering the magnetic field magnitude. For measuring the PL as a function of magnetic field (c.f. II A), we sweep from high to low field while maintaining the same orientation (without resetting).

We note that our data was acquired over the course of three distinct cooldowns. In cooldown #1, we used a different microwave antenna than the CPW discussed above, which resulted in microwave heating. Consequently, we resorted to all-optical measurements of PL during this cooldown. Cooldowns #2 and #3 were identical in terms of experimental setup and used the aluminum CPW. All contrast vs temperature data on Setup A were taken during those cooldowns. During cooldown #2, two of our NVs (NV-2 and NV-4) bleached (i.e. they showed a complete loss of spin contrast at a reduced PL level). Bringing them to ambient conditions for a short time completely restored their previous properties and they have not shown signs of bleaching since. Importantly, all our data is consistent across all three cooldowns and in line with the observations in Setup B (NV-5), which emphasizes the independence of our results from setup-related conditions.

II. MEASUREMENTS

In our work, we use five types of experiments to thoroughly characterize each NV and to disentangle the various fitting parameters. Fitting the first three experiment types (II A - II C) is a simultaneous effort, further discussed in section IV A, due to shared parameters between all of them. The fourth experiment type, namely the shelving state lifetime (II D), is determined independently. The fifth type of experiment (II E) is used to verify that we are working with the negative charge state NV^- of the NV center. This section discusses all five experiments in detail.

A. PL vs. B

We measure the steady-state PL while sweeping the magnitude of the magnetic field B from high field to low field (Fig. S1(a)). At base temperature, such a trace exhibits minima at the level anti-crossings (LAC) of the ES and the GS, which we use to uniquely characterize the in-plane strain and magnetic field alignment [15, 20].

While the relative depth of the ES LAC minima at base temperature (e.g. 30 mT and 55 mT in Fig. S1(a)) is known to depend on the ES branch-selectivity of the optical excitation [20], we find an additional dependence on the orbital hopping rate. Specifically, the spontaneous emission process $E_x \rightarrow E_y$ that is relevant in the presence of in-plane strain causes the first E_y LAC minimum to be deeper than the second E_x LAC minimum. The rate of this spontaneous emission process (c.f. Eq. S6) depends on the electron-phonon coupling strength η , which is a fit parameter in our model. To avoid cross-talk between the fit of η and the branch selectivity, we always assume no orbital branch selectivity in our optical excitation, i.e. $r_\beta = \beta_x/\beta_y = 1$ (c.f. Fig. S3). This assumption is reasonable for the following reasons: (i) we off-resonantly excite NV centers with green laser light into the phonon sideband, where the selectivity is naturally low even with aligned NV and laser polarization axes [16, 40]. (ii) our NV center principal axes are tilted by 55° relative to the diamond surface and optical axis, reducing the possible polarization alignment.

When fitting a *PL vs. B* measurement, we exclude points below 15 mT, to avoid possible distortions due to the remanent field of the vector magnet.

B. Time-resolved pulsed ODMR

We measure the time-resolved, spin state dependent PL under excitation with $\sim 2 \mu\text{s}$ laser pulses (Fig. S1(b)). After a such a laser pulse, the spin state of the NV center is initialized – with some laser power dependent fidelity [41] – into the $m_S = 0$ state. In a subsequent laser pulse, we thus obtain the time-resolved PL of the $m_S = 0$ initialized state. Likewise, if a microwave pulse that results in an adiabatic inversion of the spin state is applied beforehand, we obtain the time-resolved PL of the $m_S = -1$ initialized state. The relative difference between these two traces, integrated over the first 250 ns, results in the ODMR spin contrast. Explicitly, the contrast is calculated from the integrated counts of the $m_S = -1$ state divided by the integrated counts of the $m_S = 0$ state. We find that the contrast is fairly resilient against changes in setup-specific parameters. In addition to determining contrast, we use the raw, time-resolved PL traces to fit for the rates related to the optical lifetime and intersystem-crossing (ISC) process. We note that setup-specific parameters also change the curve shape.

C. Saturation measurement

The measurement of the steady-state PL while sweeping the laser power shows a characteristic saturation behavior that arises when the optical excitation rate exceeds the lifetime of the electronic excited state. Then, the laser power dependent PL becomes linear with a slope given by the fluorescent background (c.f. Fig. S1(c)). The laser power at which the saturation is reached is characteristic for the excitation efficiency. The absolute PL level on the other hand is characteristic for the collection efficiency. Therefore, saturation measurements are primarily suited to characterize these three setup-specific parameters (background, excitation and collection efficiency) and to disentangle them from rate parameters.

D. Shelving state lifetime

The shelving state lifetime (SSL), i.e. the time spent in the intermediate singlet levels before decaying back into the GS (c.f. Fig. 2 of the main text), has a well-known temperature dependence that we include in our model of the NV photo-physics. We measure the SSL following Refs. [30, 35], by first exciting the NV into the shelving state using a $1.2 \mu\text{s}$ laser pulse and subsequently probing the initial PL in a second laser pulse, delayed by τ . The resulting exponential rise $\text{PL} \propto 1 - ae^{-\tau/\tau_S(T)}$ can be fitted for the SSL $\tau_S(T)$ at the measurement temperature T . Obtaining such data points $\tau_S(T)$ for several temperatures allows in a second step to fit the parameters of the temperature dependence of the SSL. We fit $\tau_{S,0}$ at zero temperature from Eq. S4 for each NV center individually. The fit results are given in table I. Fitting $\tau_S(T)$ reliably for ΔE in Eq. S4 requires a significant amount of measurements in the range $T \gg 100 \text{ K}$, which was not accessible in our experiments. We therefore use the same $\Delta E = 16.6 \text{ meV}$ as reported by Robledo *et al.* [35]. In Fig. S1(d) we present the result of such an evaluation scheme at the example of NV-2.

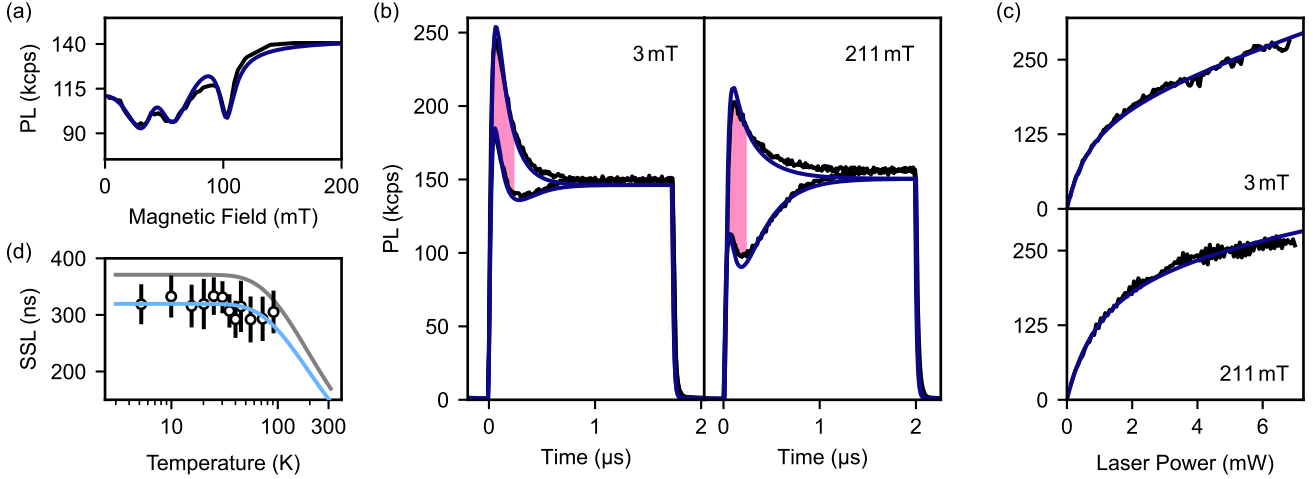


Figure S1. **Example for measurement types used in our fitting process** - Shown are complementary measurements used in this work, with their corresponding fits (solid blue lines), taken on NV-2. (a - c) were taken at base temperature (~ 5 K) and constitute a typical data set for the simultaneous fitting described in section IV A. (a) *PL vs. B* measurement. (b) *Time-resolved pulsed ODMR* at low and high magnetic field. Contrast is integrated over the pink shaded area (first 250 ns). (c) *Saturation* measurement. (d) Measurement and fit of the temperature dependence of the SSL. For comparison, the findings of Robledo *et al.* [35] are also shown (grey).

E. Continuous time tagging

At each temperature step, after all other measurements are completed, we additionally record PL during 60 s of continuous laser illumination. The raw timetags (resolution: 10 ns) are binned with a sampling rate of 10 kHz to obtain count-rate histograms as shown in Fig. S2 (for NV-1 at select temperatures). After removing noise from pulse tube vibrations (1.4 Hz) and rotary valve motor vibrations (140 Hz) and their harmonics, the histograms approximate the shot noise limit well. The strictly Gaussian nature of the signal indicates that no blinking occurred on our NVs on time scales limited by the 60 s-long measurement time on slow time-scales, and the 10 kHz sampling rate on fast time-scales. This supports our conclusion in the main text, that charge-state switching between NV^- and NV^0 is not involved in the temperature-dependent reduction of PL and contrast.

III. THE NUMERICAL MODEL

Our model is derived in detail in Ref. [23]. Here, we summarize the most important equations and relate them to our fitting algorithm.

A. Level structure and optical transition rates

We calculate the NVs energy level structure and eigenstates at a given magnetic bias field (with magnitude B , polar angle θ_B and azimuthal angle ϕ_B) and in-plane strain (with magnitude δ_\perp and azimuthal angle ϕ_δ) using the well-established low temperature Hamiltonian [28]. We neglect the hyperfine interactions and on-axis strain, as they are not relevant for this work. Angles are measured relative to the NV coordinate system in Ref. [28]. Between the calculated levels, we define transition rates to model optical excitation ($\beta_{x/y}k_r$) and relaxation (k_r , $k_{E_{12}}$, $k_{E_{xy}}$, k_{A_1}), as well as phonon-mediated spin-conserving transitions ($k_{\uparrow/\downarrow}$), as depicted in Fig. S3. To do so, it is convenient to implement the Hamiltonian in different bases and transform between them.

We assume no temperature dependence for the optical excitation k_r [39]. The intersystem-crossing (ISC) transitions from the excited state to the shelving state (SS) have been shown to be slightly temperature dependent [31, 42] at high temperature, but the effect is too small to have an impact on our model. The temperature dependence of the ISC rates below 30 K, as reported in their work, is readily contained in our model [23].

The SS relaxation, on the other hand, has a well established temperature dependence and we model it following

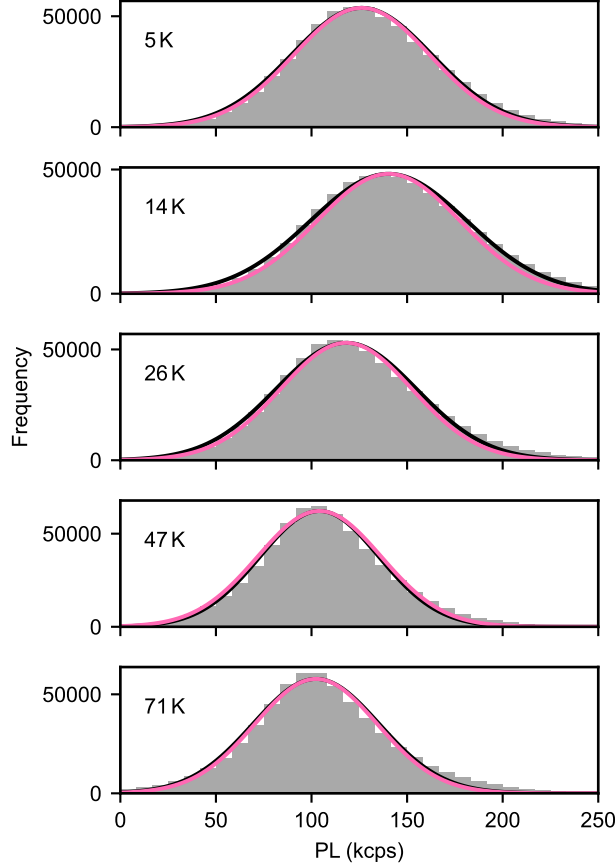


Figure S2. **Histograms of the PL count rate of NV-1 at varying temperatures** - Dilution refrigerator vibrations at 1.4 Hz and 140 Hz and their harmonics have been removed from the data. The pink curve indicates the theoretical shot noise limit of the measurement, the black line is a Gaussian fit to the histogram.

Robledo *et al.* [35]

$$\tau_S(T) = \frac{1}{k_{S0} + k_{S1}} = \tau_{S,0} \left(1 - e^{-\frac{\Delta E}{k_B T}}\right) \quad (\text{S4})$$

with a spontaneous emission process ($\tau_{S,0}$) and a stimulated emission process of a phonon with energy ΔE . Here, k_B is the Boltzmann constant and we use the literature values for ΔE (see table I). We note that the branching ratio $r_S = k_{S0}/k_{S1}$ remains approximately constant in temperature [43].

B. Orbital hopping rates

The primary effect of temperature in our model lies in the addition of hopping rates between the two orbital branches to the rate model, similar to previous studies [16, 31, 32]. This hopping is caused by one- and two-phonon-processes and thus depends on the thermal occupation of phonon modes. We introduce rates

$$\begin{aligned} E_y \rightarrow E_x : k_{\uparrow}(T, \delta_{\perp}, \eta) &= k_{\uparrow,1} + k_{\uparrow,2} \\ E_x \rightarrow E_y : k_{\downarrow}(T, \delta_{\perp}, \eta) &= k_{\downarrow,1} + k_{\downarrow,2} \end{aligned} \quad (\text{S5})$$

which depend on both temperature T and the strain induced splitting of the orbital branches, which is approximately $\approx 2\delta_{\perp}$ for a sufficiently small $g_{\perp}B_z$, as we expect for all our measurements [20]. The coupling strength between electronic orbital states of the NV^- and phonons is given by η .

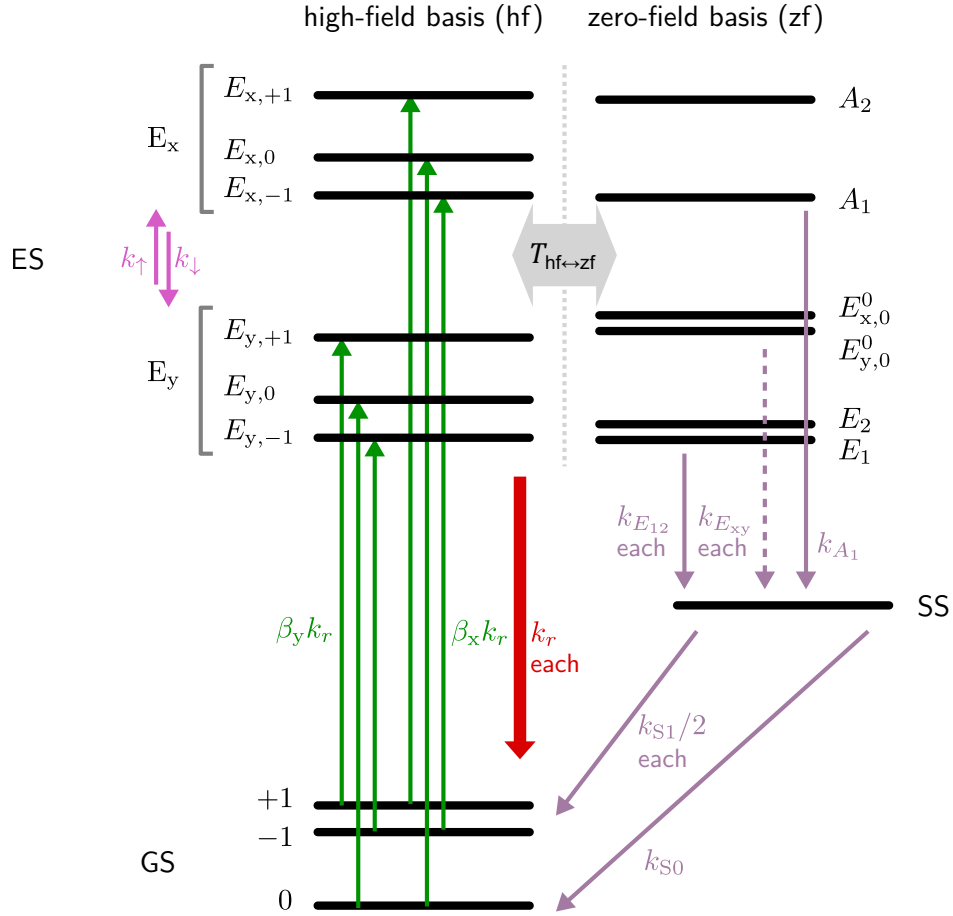


Figure S3. **Energy levels and transition rates** - Depicted are the 10 energy levels of the zero-temperature NV^- center Hamiltonian. The ES is depicted in two different bases: the high-field basis (hf) which is a good eigenbasis at high magnetic field $\vec{B} \parallel \hat{e}_z$ and high strain δ_\perp and the zero-field basis (zf), which covers the limit of $\vec{B} \rightarrow 0$ and $\delta_\perp \rightarrow 0$. Transition rates (arrows) are implemented in the basis in which they are defined and we use basis transformations to combine them into a single master equation (c.f. section III C). Optical excitation ($\beta_{x/y} k_r$) from the ground state GS to the two branches (E_x , E_y) of the excited state ES is spin m_s conserving and dependent on the excitation power and polarization (x , y). Optical decay (k_r) is also spin conserving and leads to the emission of a red photon. The ISC rates ($k_{E_{12}}$, $k_{E_{xy}}$, k_{A_1}) are dependent on the fine structure levels, which are good eigenstates in zero-field. The decay from the SS to the GS repopulates all spin states, with a branching ratio defined as $r_S = k_0/k_{S1}$. Phonon mediated, coherent spin state preserving transitions ($k_{\uparrow/\downarrow}$) between the two orbital branches occur at a rate that increases with temperature.

The expressions for the hopping rates can be derived following Fermi's Golden Rule, as is done in Refs. [23, 32, 34]. Here, we just state the results. For the one-phonon process, one finds

$$\begin{aligned} k_{\uparrow,1}(T, \delta_\perp) &\approx 32\eta h^3 \delta_\perp^3 n(2\delta_\perp h) \\ k_{\downarrow,1}(T, \delta_\perp) &\approx 32\eta h^3 \delta_\perp^3 [n(2\delta_\perp h) + 1], \end{aligned} \quad (\text{S6})$$

where the Bose-Einstein distribution $n(\epsilon)$ describes the thermal occupation of phonon modes with energy ϵ at temperature T . The rates for the opposite directions are related by detailed balance as $k_\uparrow = \exp\left(-\frac{2\delta_\perp h}{k_B T}\right) k_\downarrow$. Notably, the spontaneous emission term (“+1”) in $k_{\downarrow,1}$ results in a finite, strain-dependent rate that needs to be considered even at $T = 0$ K.

For the two-phonon process, we find

$$\begin{aligned} k_{\uparrow,2}(T, \delta_\perp) &= \frac{64\hbar}{\pi} \eta^2 k_B^5 T^5 \int_{x_\perp}^{\Omega/k_B T} \frac{e^x x (x - x_\perp) [x^2 + (x - x_\perp)^2]}{2(e^x - 1)(e^{x-x_\perp} - 1)} dx \\ &= \frac{64\hbar}{\pi} \eta^2 k_B^5 T^5 I(T, \delta_\perp), \end{aligned} \quad (\text{S7})$$

where x is the phonon energy in units of $k_B T$ and $x_\perp \approx \frac{2\delta_\perp \hbar}{k_B T}$. In the second line, we introduced the temperature- and strain-dependent integral over the phonon modes $I(T, \delta_\perp)$. Using the detailed balance, one can directly obtain $k_{\downarrow,2}(T, \delta_\perp)$.

C. Master equation

Importantly, the orbital hopping rates $k_{\uparrow/\downarrow}$ only act on the orbital subspace, leaving the state in the spin subspace untouched. This cannot be modeled by a classical rate equation model as is commonly used. We therefore employ a master equation model that acts on quantum states but can include the known classical rates via jump operators. We numerically calculate the time evolution of the 10-dimensional density matrix ρ (including the three GS states, six ES states and the SS) using the Liouville equation

$$\frac{d}{dt}\hat{\rho} = -\frac{i}{\hbar}[\hat{H}, \hat{\rho}] + \sum_k \left(\hat{L}_k \hat{\rho} \hat{L}_k^\dagger - \frac{1}{2} \{ \hat{L}_k^\dagger \hat{L}_k, \hat{\rho} \} \right) \equiv \mathcal{L}(\rho). \quad (\text{S8})$$

Details on the implementation of the jump operators can be found in Ref. [23].

D. Linking simulation with experiment

The quantity we observe in our experiments is always the PL averaged over some time or many repetitions of a sequence of laser and microwave pulses. The PL is composed of radiative emission of the NV^- center and fluorescent background radiation. We assume a linear dependence of the background PL on the laser power. The collected PL can be calculated from the populations $\rho_{i,i}$ of the emitting levels, which have the same indices $i \in [4, 9]$ for all bases. We thus model the observed PL as:

$$\text{PL}(t) = AR \left(\sum_{i \in [4,9]} \rho_{i,i}(t) k_r \right) + bP \quad (\text{S9})$$

where we introduce a set of setup-related parameters. A represents the optical excitation efficiency (unit: W^{-1}), which can drift over time and change from experiment to experiment if setup conditions are not stable enough. R is the ratio of collection over excitation efficiency (unit: cps W s) and is expected to be fairly stable against drifts in the optical path. Lastly, b characterizes the background counts (unit: cps W), which are linear in the laser power P .

To simulate and fit the time-resolved PL response of NV centers in our setup as given in Fig. 1(a) of the main text, we need to take the rise time of our laser pulses into account. Thus, we introduce the laser rise time τ_R to our model, the value of which we determined experimentally. This is necessary when fitting $\text{PL}(t)$ time traces as τ_R of our laser is longer than the time resolution of our photo-detector (10 ns). In the derivation of our model we assume a time-independent Liouvillian superoperator \mathcal{L} in the Liouville equation S8. The laser power P enters into \mathcal{L} in the form of a pre-factor of the jump operators describing the optical excitation. We thus need to ramp up the laser power and thus \mathcal{L} in N discrete steps

$$P(t) = \begin{cases} 0 & \text{if } t < t_0 \\ P \left(1 - e^{-\frac{t-t_0}{\tau_R}} \right) & \text{for } t_n = \left\lceil \frac{t-t_0}{\Delta t} \right\rceil \Delta t \\ P & \text{if } t > t_0 + N\tau_R \end{cases} \quad (\text{S10})$$

and use fix parameters $N = 4$ and $\Delta t = 5$ ns here. We find that the influence of τ_R on the spin contrast is negligibly small. In fitting time-resolved pulsed ODMR traces, on the other hand, τ_R is crucial. Likewise, we need to determine the precise value of t_0 individually for each measurement. This is done by a linear extrapolation to $\text{PL} = 0$ from the first two data points above the dark count level, which we also determine and include in the model.

E. Evaluating sensing performance

In this work, we aim to give a direct comparison of the performance of the NV^- center as a sensor over a vast range of parameters. To that end, it is necessary to compare the optimized performance for each parameter setting, as done

in section V A. We optimize the integration time of simulated pulsed ODMR experiments, which are representative for all kinds of sensing schemes. We note though, that also the laser power could be optimized, which is beyond the scope of this work. In the following, we give a brief derivation of the sensitivity and its relation to the SNR.

We assume a pulsed ODMR experiment to measure the magnetic field component along the NV axis [44]. The sensitivity $s = \Delta B_{\min} \sqrt{t}$ is then given by the minimal magnetic field change ΔB_{\min} , that can be measured within time t . The microwave frequency f dependent photon counts signal \mathcal{S} has the shape of a Gaussian with

$$\mathcal{S}(f) = \left[1 - e^{-4 \ln(2)(f-f_0)^2/\nu^2} \right] \mathcal{S}_{m_S=0},$$

where f_0 is the resonance frequency at which a pi-pulse between the spin levels can happen, and ν is the full width half maximum (FWHM) of the Gaussian (and related to the inverse spin coherence time). The \mathcal{S} ($\mathcal{S}_{m_S=0}$) are the total collected counts during t that fall into the integration window t_{int} with (without) a microwave pulse applied before the laser pulse (c.f. Fig. S1(b)). Since f_0 shifts with the magnetic field as $\Delta B = \Delta f 2\pi/\gamma = \Delta f/28.025 \text{ MHz mT}^{-1}$, best (i.e. smallest) sensitivity is achieved at the frequency f_s of highest slope of $\mathcal{S}(f)$. At this frequency, a pulsed ODMR experiment is performed, repetitively consisting of a pi pulse and a subsequent laser pulse for readout and re-initialization. Assuming a shot noise $\Delta \mathcal{S} = \sqrt{\mathcal{S}}$ limited readout at f_s , one finds for the sensitivity

$$s = \frac{2\pi}{\gamma} m_G^{-1} \frac{\nu \sqrt{r_G}}{C \sqrt{\text{PL}_{m_S=0} \sqrt{\text{DC}}}}. \quad (\text{S11})$$

Due to the Gaussian shape, $m_G^{-1} = 0.700$ and $r_G = 1 - 0.607 \cdot C$. Further, $\text{PL}_{m_S=0} = \mathcal{S}_{m_S=0}/(t_{\text{int}} N_{\text{seq}})$ is the average PL count rate during t_{int} , with $N_{\text{seq}} = t/T_{\text{seq}}$ the number of repetitions of the pulsed ODMR sequence of duration T_{seq} . Finally, the readout duty cycle $\text{DC} = t_{\text{int}}/T_{\text{seq}}$ and the spin contrast $C = 1 - \mathcal{S}(f_0)/\mathcal{S}_{m_S=0}$.

Viewing the readout of the spin state in a generalized and ideal scheme [45] a similar result of

$$s \propto \text{SNR}^{-1} \propto \frac{\sqrt{r}}{C \sqrt{\text{PL}_{m_S=0}}} \quad (\text{S12})$$

can be found for the sensitivity and SNR. Here, $r = 1 - 0.5 \cdot C$.

In simulations with optimal readout, we optimize Eq. S11 at every parameter setting for the t_{int} that gives best sensitivity. Explicitly, this yields not the t_{int} with highest contrast. For a more intuitive picture, the inverse sensitivity and SNR are approximately proportional to

$$\text{SNR} \sim C \sqrt{\text{PL}_{\text{ss}}}, \quad (\text{S13})$$

with the quantities spin contrast C and steady-state PL (here called PL_{ss} for clarity) used elsewhere in this work.

IV. DATA FITTING AND SIMULATION

In this section, we describe how we fit our measurements to calibrate the model and then, subsequently, simulate the NV PL to compare the theory to our measurements. When fitting, we distinguish two primary sets of fit parameters. The first set, the *robust* parameters, includes all NV-intrinsic parameters (i.e. strain and rates) and the magnetic bias field, which we have good control over. These parameters are stable against scanning stage movements and other drifts which can occur between measurements, particularly when changing to a new temperature or magnetic field. The second set, the *environment-sensitive* parameters, is prone to change between measurements. They include the setup parameters discussed in section III D. These definitions help to distinguish the following three processes:

- *Calibration*: Simultaneous fit of multiple data sets across multiple temperatures T_i and fields B_i with common *robust* parameters but unique *environment-sensitive* parameters for each T_i/B_i . The procedure is described in great detail in the next section IV A.
- *Simulation*: Uses the calibration-results for the *robust* parameters and a *single* set of *environment-sensitive* parameters to effectively extrapolate the NV photo-physics to the full range of temperature, magnetic field and strain. This is used, for example, in contrast vs. temperature curves (c.f. Fig. 1(b) in the main text) and in maps of PL vs. B vs. T (c.f. Fig. 3(a)). Deviations from experimental data are found, particularly at high temperatures where drifts become significant.
- *Fits*: Fits use the calibration-results for the *robust* parameters but exclusively re-fit the *environment-sensitive* parameters to a given data set at a specific (T, B) . This effectively corrects for experimental drifts. Examples are fits of PL vs. B (c.f. Fig. 3(b)) measurements and PL traces (c.f. Fig. 1(a)).

A. Calibration

The NV center Hamiltonian that we use in our model contains eight fundamental constants describing the various interactions that yield its spin and electronic eigenstates at zero temperature. We use recent literature values for these [15, 28, 36, 37] and assume them to be the same for all conditions. Apart from those constants, there are several other parameters in the model: (i) NV center specific crystal strain parameters, (ii) magnetic bias field related parameters, (iii) rates, (iv) electron-phonon interaction, and finally (v) setup specific parameters. A subset of those parameters is fixed during the complete calibration process described below, either because they are *predetermined* from separate measurements (e.g. laser rise time) or because they are taken from literature. An overview of all parameters (fitted and fixed) and their respective categorization (robust, environment-sensitive, predetermined, literature) is given in Tab. I.

We perform the fitting in three stages (I-III), where each stage informs the set of initial parameters of the subsequent fit. This ensures good convergence despite the vast number of parameters.

(I) We start by fitting a *PL vs. B* measurement at base temperature ($\sim 5\text{K}$) to our full model. We fit for the in-plane strain (δ_{\perp} , ϕ_{δ}) and magnetic field alignment (θ_B , ϕ_B) as well as the setup-specific parameters (b , R , A). We use common literature values for all other parameters.

(II) We then simultaneously fit a data set consisting of five different measurements at base temperature, with all parameters being fitted (except for η). This data set includes (i) the *PL vs. B* from before, (ii) two *time-resolved pulsed ODMR* traces and (iii) two *saturation* measurements at low (3 mT) and at high (200 mT) magnetic field. Such a data set for NV-2 is shown in Fig. S1.

(III) Finally, we fit the same base-temperature *PL vs. B* together with 6 (5 for NV-4) pairs of *time-resolved pulsed ODMR* and *saturation* measurements, sampled across our full temperature range. This allows us to fit for the electron-phonon coupling strength η , in addition to a final fine-tuning of the full parameter set. Crucially, we use a common set of *robust* parameters across all data sets, but individual *environment-sensitive* parameters are used for each data set, which account for mechanical drifts in the experimental setup. Specifically, the two parameters background b and collection over excitation ratio R are fitted separately to each pair of *saturation* and *time-resolved pulsed ODMR* measurements (at the same field and temperature) and also separately to the base-temperature *PL vs. B* measurement. Further, the alignment parameter A has to be fitted separately for every single measurement. This results in a total of 60 fit parameters simultaneously fitted to 25 distinct measurements.

We find that the simultaneous fit of these 25 measurements in stage (III) improves the stability of the fit compared to stage (II) containing only the five base temperature measurements. Particularly, the in-plane magnetic field angle, which results from finite misalignment, can have little observable effect on the PL at base temperature but plays a more significant role at higher temperature.

B. Calibration results

Results of the calibration for the different NV centers are presented in Tab. I and Fig. S4. The latter contains the *environment-sensitive* parameters that have been determined across all temperatures, as described above. For NV-1 we were not able to include *saturation* measurements in the fit as the PL stability required here was not sufficient. We stress that the fitted setup-parameters do not show a correlation with temperature. In particular, in Fig. S4 we do not see any feature at $\sim 30\text{K}$, the location of the contrast and PL minimum.

Since cooldown #1 has different magnetic field alignment due to changes in the setup, a different in-plane magnetic field angle was used for the *PL vs. B* measurement at base temperature if fitted simultaneously with measurements from cooldown #2 and #3 – this is the case for NV-2 and NV-1. Based on our measurements, we can only determine the in-plane magnetic field and strain angle relative to one out of three possible crystal axes, which we then call the x -Axis of our coordinate system [28]. Moreover, we do not know the sign of the z -Axis. Therefore, given the three-fold rotational symmetry and mirror symmetry to the xz -plane, we choose to determine values for the in-plane strain angle in the range $[0^{\circ}, 60^{\circ}]$. The in-plane magnetic field angle can then have any orientation relative to it, i.e. covers a range of $[0^{\circ}, 360^{\circ}]$.

We compare the calibration results of select parameters to literature values in table II. First, we note that our SS branching ratio r_S fits well into the broad range of values obtained in other experiments. It appears that r_S varies substantially between NV centers even within individual studies. Theoretical modelling prefers a higher $r_S \approx 6$ [43] than measured in many of those works, including ours. The cause for this disparity is unknown, and no significant strain or temperature dependence has been observed to date. This represents an open question that will have to be addressed with suitable measurement techniques in future work.

		NV-1	NV-2	NV-3	NV-4	
Strain						
δ_{\perp}	ES in-plane strain (GHz)	31.8	39.9	8.7	80.2	<i>a</i>
ϕ_{δ}	ES in-plane strain angle	39.9°	24.4°	0.8°	59.9°	<i>a</i>
Magnetic bias field						
θ_B	mag. field alignment angle	1.7°	1.9°	1.8°	2.2°	<i>a</i>
ϕ_B	mag. field in-plane angle	244.0°	17.6°	106.5°	130.6°	<i>a</i>
ϕ_B	cooldown #1	256.2°	194.2°			<i>a</i>
Rates						
k_T	opt. emission rate (μs^{-1})	55.1	55.7	45.3	40.5	<i>a</i>
$k_{E_{12}}$	ISC rate from $E_{1,2}$ (μs^{-1})	112.4	98.7	101.3	90.7	<i>a</i>
k_{A_1}	ISC rate from A_1 (μs^{-1})		$k_{E_{12}}/0.52$ [31]			<i>d</i>
$k_{E_{xy}}$	ISC rate from $E_{x,y}$ (μs^{-1})	9.1	8.2	8.6	7.5	<i>a</i>
$r_{\beta} = \beta_x/\beta_y$	opt. exc. branching ratio		1			<i>c</i>
$r_S = k_{S0}/k_{S1}$	SS branching ratio	1.36	2.26	1.44	1.15	<i>a</i>
$\tau_{S,0} = 1/(k_{S0} + k_{S1})$	SS decay time at $T = 0$ K (ns)	342	320	292	318	<i>c</i>
ΔE	SS emit. phonon energy (meV)		16.6 [35]			<i>d</i>
Electron-phonon interaction						
η	ES coupling strength ($\mu\text{s}^{-1} \text{meV}^{-3}$)	197	176	268	249	<i>a</i>
Ω	phon. cutoff energy (meV)		168			<i>d</i>
Setup - Base temperature PL vs. B measurement						
b	background (kcps mW^{-1})	40.8	27.5	52.6	34.7	<i>b</i>
R	$\frac{\text{collection}}{\text{excitation}}$ efficiency (kcps $\text{mW} \mu\text{s}$)	67.1	88.4	112.1	178.3	<i>b</i>
A	opt. alignment (W^{-1})	245.1	136.2	282.3	188.1	<i>b</i>
τ_R	laser rise time (ns)		23			<i>c</i>

Table I. **Calibration results per NV center** - We fit the NV center intrinsic parameters individually for each center since they are known to vary between NV centers [28]. The fit results for setup related parameters of saturation and time-resolved pulsed ODMR measurements of the same simultaneous fits are presented in Fig. S4. The last column specifies the type of parameter: (a) robust parameters, including NV intrinsic properties and the well-controlled magnetic bias field; (b) environment-sensitive parameters, which include optical excitation and collection efficiencies; (c) pre-determined parameters; (d) literature values (Hamiltonian parameters not shown). The latter two (c, d) are fixed when fitting for (a) and (b).

Reference	SS branching ratio r_S	Reference	ES coupling strength η ($\mu\text{s}^{-1} \text{meV}^{-3}$)
this work	1.15 – 2.26	this work	176 – 249
Tetienne <i>et al.</i> [19]	0.0 – 1.9 †	Plakhotnik <i>et al.</i> [32]	144
Robledo <i>et al.</i> [35]	1.1 – 2.0	Abtew <i>et al.</i> [17]	149
Gupta <i>et al.</i> [46]	2.0 – 2.3	Goldman <i>et al.</i> [31]	276
Kalb <i>et al.</i> [47]	2.0 – 8.0 †		
Wirtitsch <i>et al.</i> [41]	13.3		

Table II. **Comparison to literature values** - Our calibrated values of r_S (left) and η (right) are compared to measurement values from other studies. For each study, we give the maximum parameter range (where applicable), considering measurement error and measurements on multiple NVs. Values denoted with † were transformed from a 7-level system convention to the 5-level system used in this work.

Second, our measured electron-phonon coupling strength η falls right into the already established parameter range in literature, validating our measurement approach.

C. Simulations and fits

From the fitting process described above, we obtain all quantities needed to model the PL and contrast of each NV center in dependence of temperature, magnetic field, and strain. When performing these simulations, we fix the *environment-sensitive* parameters to values obtained at base temperature. For *PL vs. B*, these are the values given at the bottom of table I. For contrast simulations, we use the lowest-temperature values in Fig. S4 at the respective magnetic field. Based on this set of parameters, we perform simulations of PL and contrast at all temperatures.

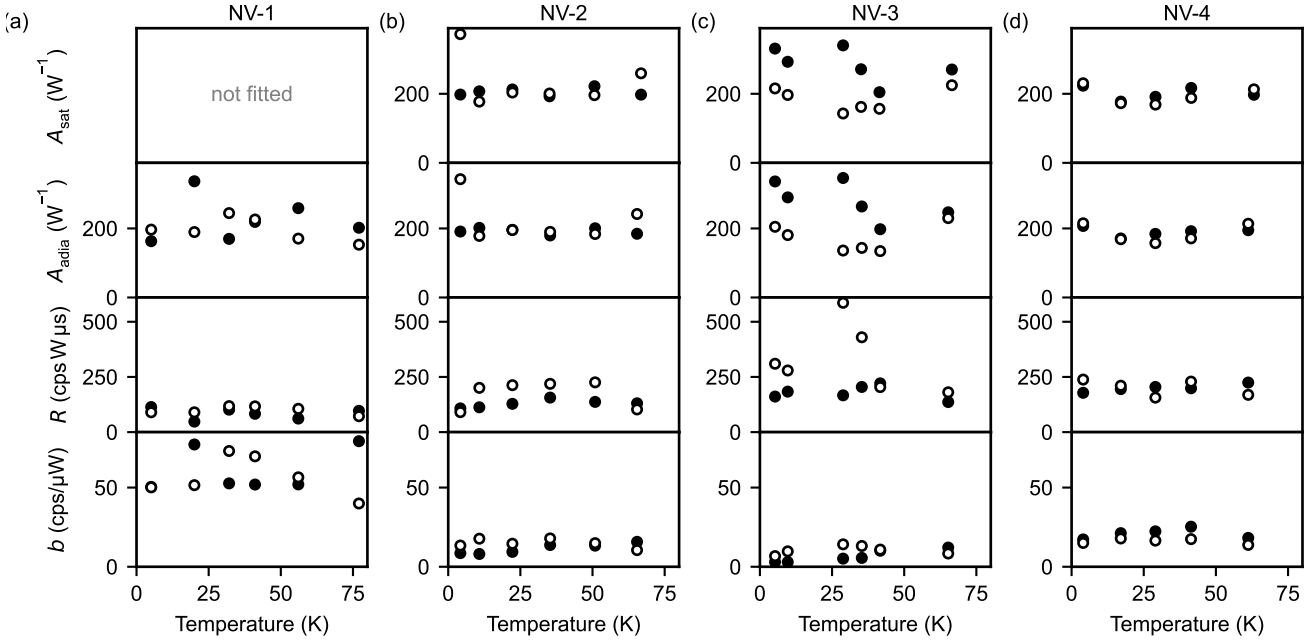


Figure S4. **Calibration results for the *environment-sensitive* parameters per NV center** - Shown are the results for the *saturation* (“sat”) measurements and *time-resolved pulsed ODMRs* (“adia”) at low (3 mT, empty circles) and at high (200 mT, filled circles) magnetic field. Temperature-independent results of the same calibration per NV center are given in Tab. I. Shown here are the optical alignment A , the ratio of collection over excitation efficiency R (common to both “sat” and “adia”) and background b (also common to both).

For PL vs. B , this process results in the maps shown in Fig. 3(a) in the main text for NV-1 and Fig. S5(a-c) for all other NVs. The maps emphasize the rich strain-dependence of the PL. We also note that when comparing the similarly-strained NV-1 and NV-2 (Fig. S5(b)), we predict a feature in the form of a small peak at ~ 50 mT and ~ 50 K in the map of NV-2 which arises due to a different in-plane strain angle ϕ_δ [23].

We performed PL vs. B measurements at select temperatures covering all three regimes (I-III) discussed in the main text, which we can compare with the theory by only refitting the *environment-sensitive* parameters b and R , while otherwise using results of the calibration. This has approximately the same effect as defining a scaling and an offset on our PL data and thus corrects for setup drifts. We find good agreement between measurement and fits for all NVs (Fig. 3(b) of the main text and Fig. S5(d-f)). We were, however, not able to resolve some small features such as the peak predicted for NV-2, likely due to a combination of remanent field effects, drift in setup parameters during one sweep, and pulse-tube vibration noise limiting our resolution of PL. We assumed the same magnetic field alignment for all measurements, i.e. we exclusively use the magnetic field orientation from the calibration fit. However, some drift and/or hysteresis of the vector magnet becomes apparent from the mismatch between data and fit in the width of the dips at the the ground state LAC (~ 100 mT) in Fig. S5(d).

To perform simulations of contrast versus temperature, we simulate and evaluate *time-resolved pulsed ODMR* sequences at the desired temperatures. In the main text, we find a good match between our simulation and the measurement data, despite the fact that the simulation uses fixed *environment-sensitive* parameters, whilst we find significant variation in the calibration at different temperatures (Fig. S4). This emphasizes the great stability of contrast measurements against setup drifts.

Finally, for Fig. 1(a) of the main text we use the parameters of the calibration and only (re-)fit the *environment-sensitive* parameters of the time-resolved pulsed ODMR traces shown in Fig. 1(a) together with their respective saturation measurement (with shared b and R and individual A as done in the calibration above).

D. Influence of the phonon model on our simulation

As mentioned in the main text, the temperature dependence of the orbital hopping rate is still under debate [43]. In Ref. [23] we give a detailed discussion of the usage of our model as a novel tool to investigate the nature of contributing phonon modes. Here, we aim to put our findings in context with previous studies.

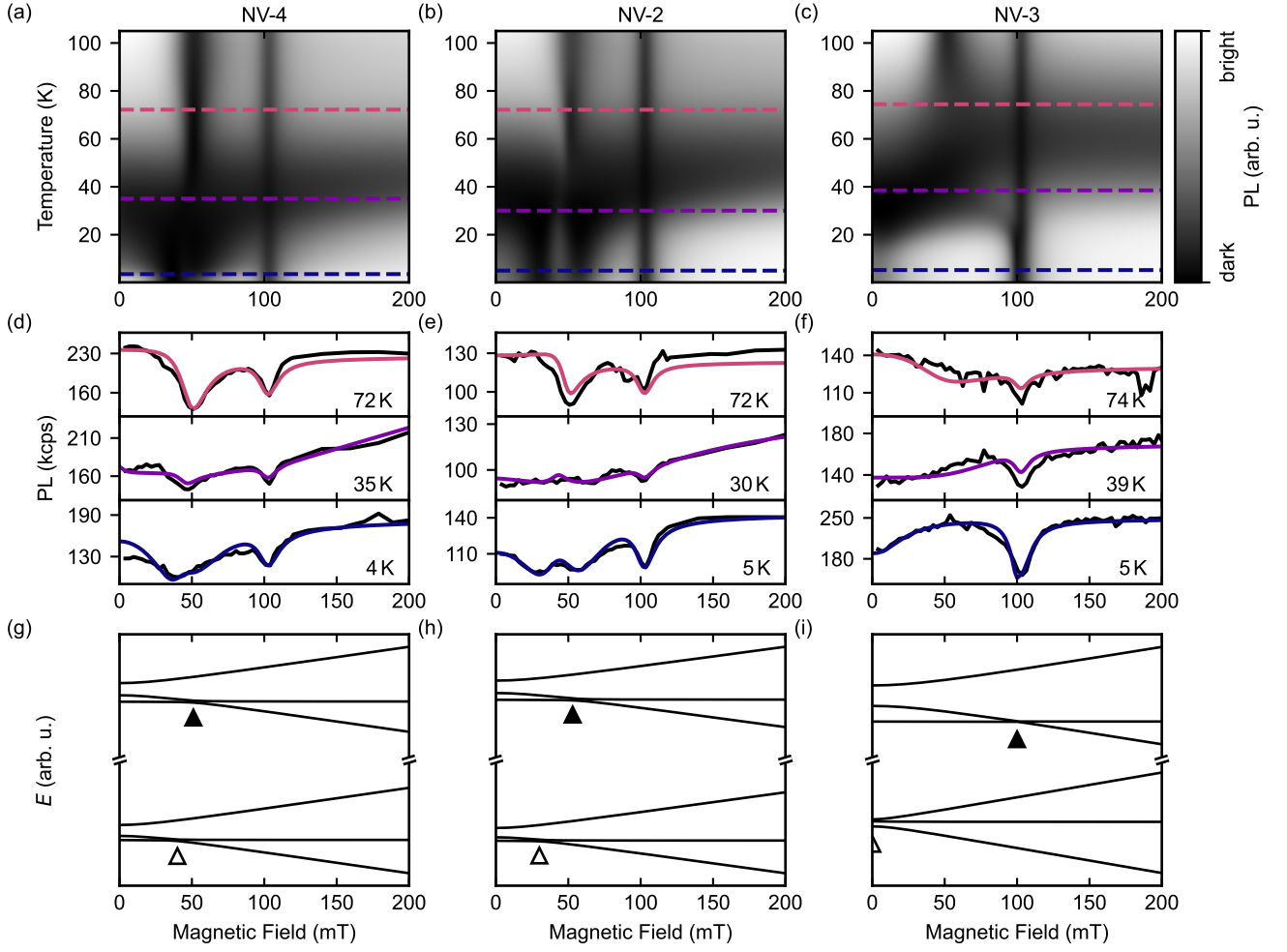


Figure S5. **Temperature dependence of the steady-state PL intensity** - Corresponding to Fig. 3 of the main text. Shown are simulations (a-c), measurements with fits (d-f) and level structures (g-i) for NV-4, NV-2, and NV-3, respectively.

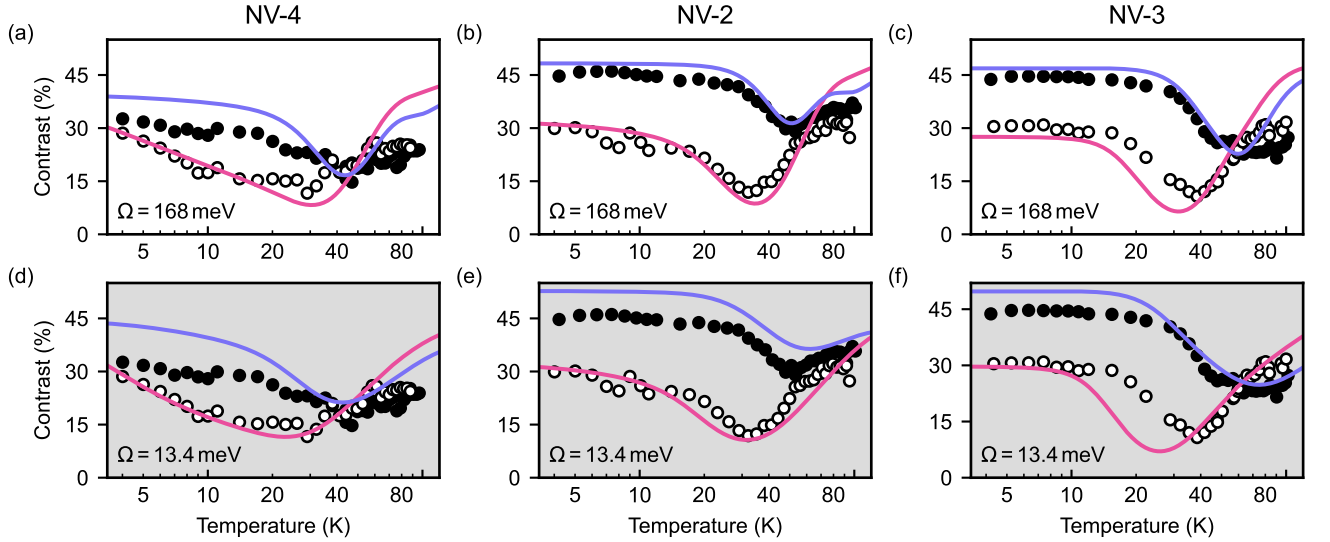


Figure S6. **Comparison between different cut-off energies** - Shown are simulations of temperature-dependent contrast (solid lines) of NV-4, NV-2, and NV-3, with two different phonon cut-off energies Ω . For (a-c) $\Omega_D = 168$ meV as in the main text, for (d-f) $\Omega_P = 13.4$ meV [32]. Empty (filled) circles are the same measurement data taken at 3 mT (200 mT) as presented in Fig. 3(e) of the main text.

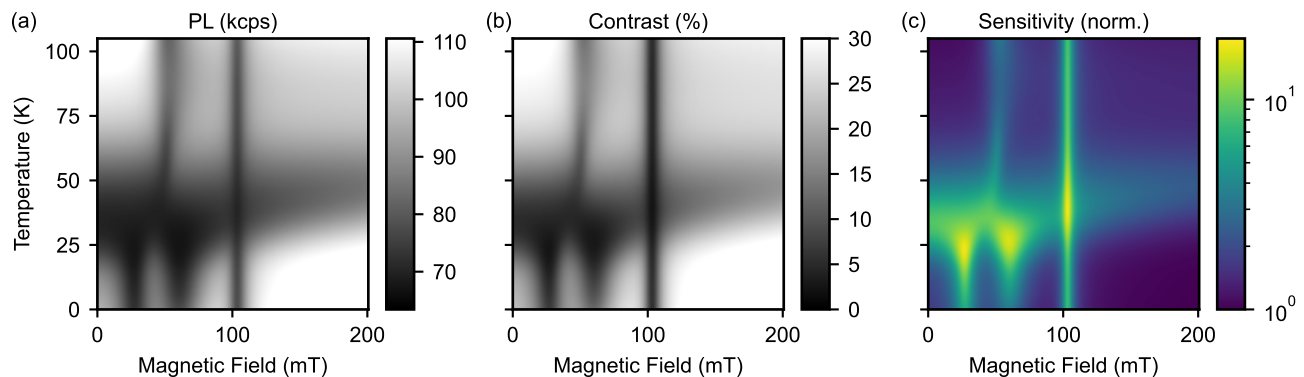


Figure S7. **Comparison of PL, contrast and sensitivity** - Shown are simulated maps of the steady-state PL (a) (same data as Fig. 3(c) of the main text), spin contrast C (b) and normalized sensitivity $s \propto \text{SNR}^{-1}$ (c) for parameters of NV-1. All show qualitatively the same behavior. Since $s \sim (C\sqrt{\text{PL}})^{-1}$, the strong variations in the NV centers sensitivity become apparent when combining (a) and (b), with its vast implications for measurements at intermediate temperatures.

We have already found good agreement of our fitted electron-phonon coupling strength η with literature values (c.f. Table II). However, we note that in all of these studies, different assumptions about the contributing phonon modes were made. In particular, the integral over the phonon spectrum $I(T)$ for the two-phonon process (c.f. Eq. 2 of the main text or Eq. S7 here) was in all cases solved in the Debye approximation but with a different phonon cut-off energy Ω . In this work, we assumed the Debye temperature of diamond ($\Omega_D = 168$ meV) as the cut-off energy. But in a study by Plakhotnik *et al.* [32], a much lower value of $\Omega_P = 13.4$ meV was found.

To investigate the effect of such a low cut-off energy, we use the value of Ω_P in our model and repeat the calibration of section IV A. As expected, it significantly alters the model, yielding higher fit results of η (NV-2: $284 \mu\text{s}^{-1} \text{meV}^{-3}$, NV-3: $512 \mu\text{s}^{-1} \text{meV}^{-3}$, NV-4: $427 \mu\text{s}^{-1} \text{meV}^{-3}$) and a slower recovery towards room temperature. Comparing the fits in Fig. S6, we find that using Ω_D yields better results at low temperatures and high magnetic fields, while – due to the slower recovery – Ω_P matches the high temperature data slightly better. Thus, presumably due to the setup instabilities and uncertainty in temperature calibration at high temperatures in Setup A (see section I), the data presented in this work does not allow to definitely rule out either of the models. In the main text we exclusively present data fitted with Ω_D , since the overall match appears better and the fitted coupling constant η agrees well with literature values. We did not attempt to fit Ω in this work and expect that the correct phonon spectrum has to be used rather than a Debye model with fitted cutoff energy Ω . For future experiments, we expect a more stable contrast versus temperature measurement in the range 80 K to 150 K to give valuable insight into the contributing phonon modes.

V. ADDITIONAL SIMULATIONS

A. Contrast, PL and sensitivity

In the main text we interchangeably used the PL and the contrast to observe or simulate the temperature dependent photo-physics of the NV center. In Fig. S7(a,b) we give a direct comparison of the temperature and magnetic field dependence of these two observables, demonstrating that they qualitatively show the same behavior. Moreover, in Fig. S7(c) we show the corresponding sensitivity, a measure for the inverse signal-to-noise ratio (SNR) when using the NV center as sensor. In good approximation, it is inversely proportional to the contrast times the square root of the steady-state PL (Eq. S11). Since both quantities are affected significantly by the spin relaxation process discussed in this work, the resulting sensitivity is impaired by more than a factor of 10.

B. Optimal integration time

Since the NV center's photodynamics change with temperature, magnetic field, and strain, the integration time for optimal sensitivity in e.g. a pulsed ODMR measurement also changes. To reduce complexity, we chose to use the

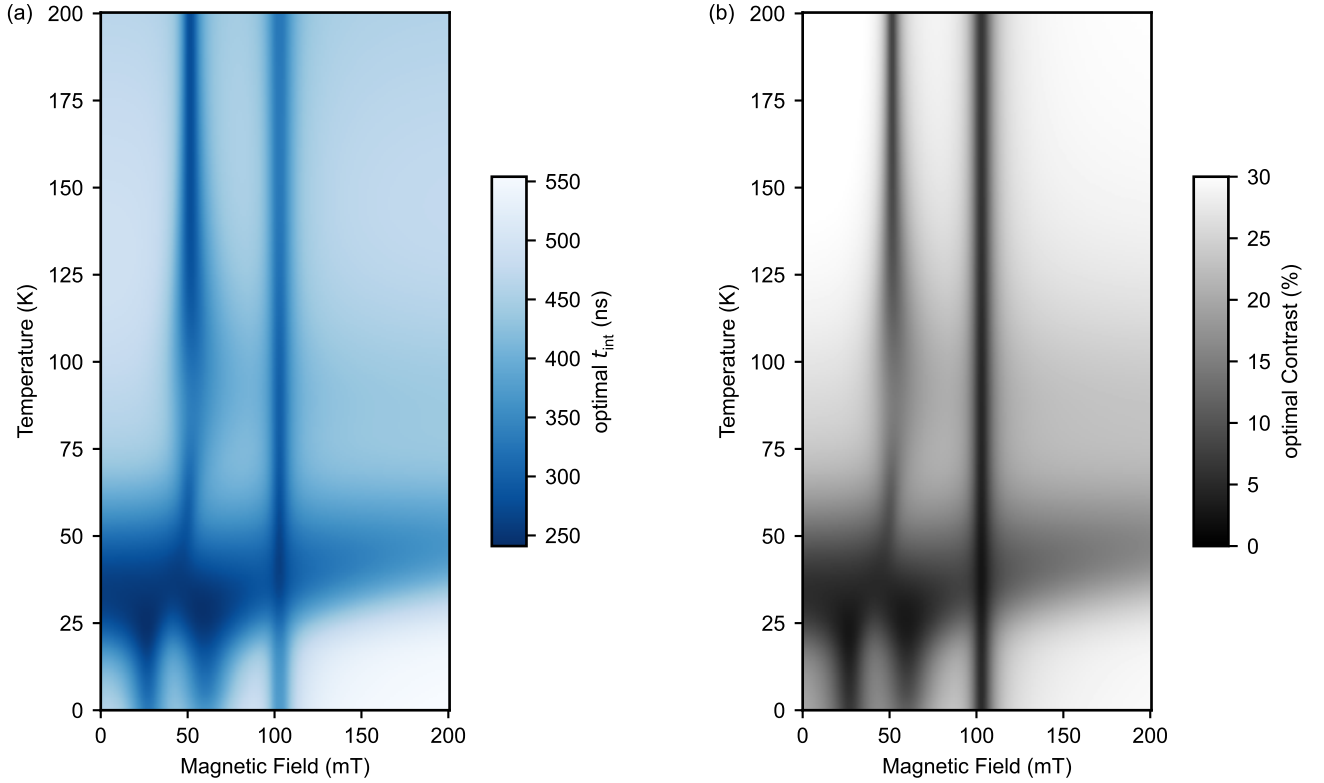


Figure S8. **Optimal integration time for NV-1** - (a) At each field and temperature a simulated pulsed ODMR was optimized for best sensitivity (Eq. S11) and the resulting integration time is plotted. (b) Corresponding spin contrast map. Both maps shows the same pattern as they are dominated by the same spin relaxation process addressed in this work. Spin relaxation in the ES leads to a faster loss of ODMR spin contrast under laser illumination, promoting a shorter integration time. For comparison, the same contrast map for $t_{\text{int}} = 250$ ns is given in Fig. S7(b). While, as expected, a change of t_{int} changes the absolute contrast value, the qualitative behavior is unaffected.

same integration time of 250 ns at all conditions. The effect of an integration time optimized for best sensitivity (for details see Eq. S11) at the respective conditions has no influence on the qualitative behavior, as shown in Fig. S8.

C. Spin initialization and readout fidelity

The temperature dependent spin relaxation process discussed in this work affects both, the spin state initialization (by laser illumination) as well as the spin state readout (as e.g. in pulsed ODMRs presented in Fig. 1(a) of the main text). The spin contrast as presented in this work suffers from a combination of both. To illustrate the effect of the spin relaxation process on the initialization and readout individually, we plot them separately in Fig. S9.

D. Extrapolation to low strain or high magnetic field

As discussed in the main text, very high magnetic fields are required to completely suppress the detrimental effect of spin mixing at intermediate temperature. This can be seen in Fig. S10(a) on a map of the NV center sensitivity up to 5 T. Further, the main text claims that the dip in performance at intermediate temperature is common to all NV centers. To that end, we plot in Fig. S10(b) the sensitivity for an NV center that has very low strain, as found in bulk diamond samples. We plot sensitivity instead of PL or spin contrast here, as it is proportional to the inverse SNR and therefore the relevant quantity when comparing the performance of the NV^- center under different conditions. In section III E, a brief derivation of the sensitivity relation (Eq. S11) used here is provided.

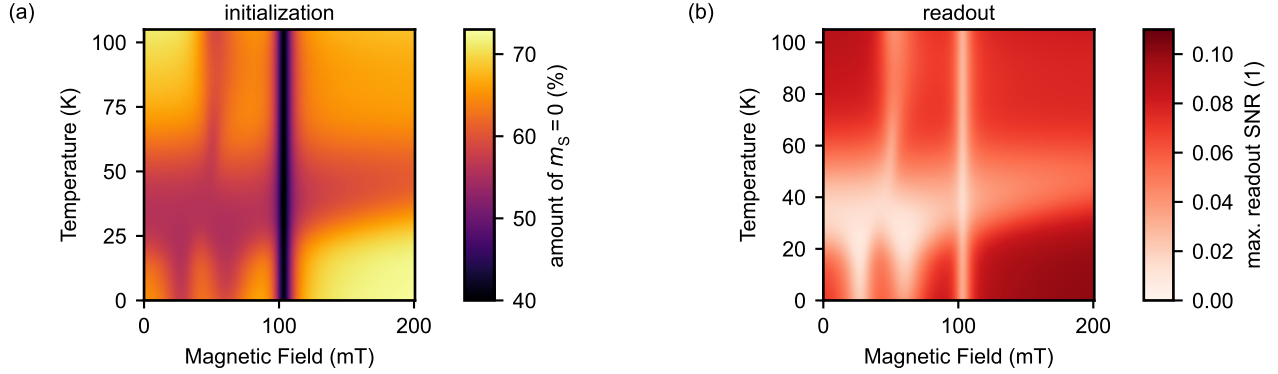


Figure S9. **Effect on spin state initialization and readout** - (a) Simulated map of the amount of $m_S = 0$ after a long green laser pulse followed by a long waiting time (no spin state T_1 process is present). This is a common scheme to initialize the spin state of the NV center. (b) Simulated maximal signal-to-noise ratio of a single spin state readout [23]. For this simulation we assumed a perfect initialization with an amount of $m_S = 0$ of 1. The integration time t_{int} was optimized at each point for maximal signal-to-noise ratio of the readout, which is almost identical to optimizing it for best sensitivity as done in Fig. S8(a) (c.f. Eq. S12). The combination of both (a) and (b) give rise to the reduced performance presented in Fig. S7. Parameters of NV-1 were used.

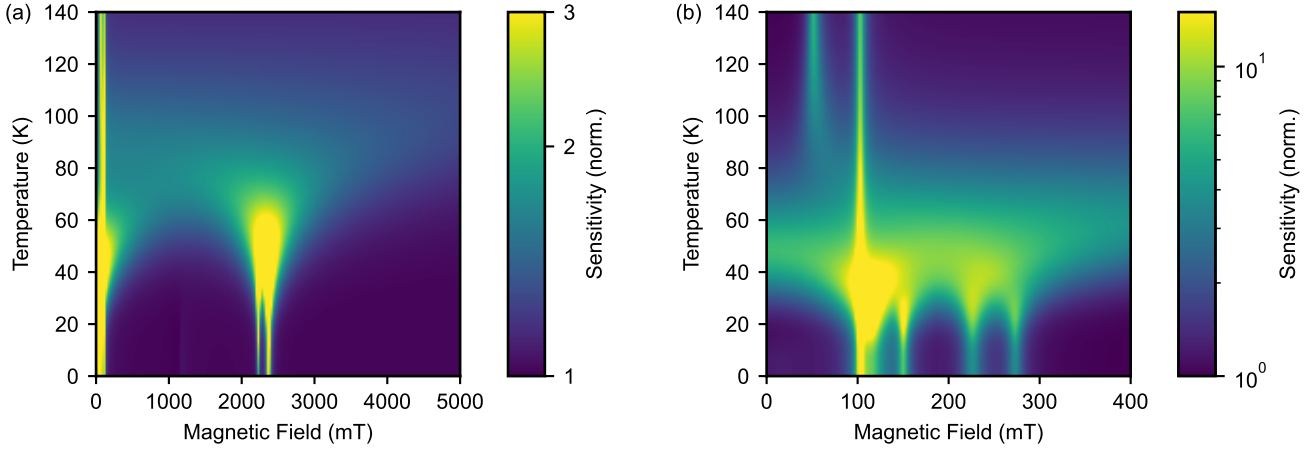


Figure S10. **Model predictions for extreme cases** - (a) Normalized sensitivity map for parameters as found for NV-1 extended to very high magnetic field. Only when approaching ~ 5 T, the dip in performance at intermediate temperatures gradually disappears. We note though, that this field value is significantly influenced by the position of the LACs above 2 T, which where observed to be shifted to significantly higher fields supposedly due to a strain dependent orbital g factor [20]. (b) Normalized sensitivity map for a NV center with very low strain splitting of 1 GHz ($\delta_{\perp} = 0.5$ GHz) as found in bulk diamond. Apart from the strain, parameters are as found for NV-1. The same qualitative behavior is observed as discussed in the main text, though the dip in performance is shifted to higher temperature. For both plots, the integration time was optimized for best sensitivity at each field and temperature for a comparison of performance.

VI. SPIN MIXING AMPLITUDES

In the main text, we introduce the spin mixing amplitude $\epsilon_{|i\rangle,|j\rangle}$ to describe the superposition between two basis states, where one of them contributes only a small amount. In a Bloch sphere picture, this amounts to only a small inclination from one of the poles (where the poles are given by the two basis states) [23]. In this picture, the new eigenstate $|\text{es}\rangle$ is given by

$$|\text{es}\rangle = |i\rangle + \epsilon_{|i\rangle,|j\rangle} |j\rangle. \quad (\text{S14})$$

The new state $|\text{es}\rangle$ is not properly normalized, but for sufficiently small $\epsilon_{|i\rangle,|j\rangle}$, this is a good approximation of the actual eigenstate $|\tilde{\text{es}}\rangle$. We calculate the $\epsilon_{|i\rangle,|j\rangle}$ by projecting the basis states onto the various eigenstates, such that

$ \epsilon_{ i\rangle, j\rangle} ^2$	$ x\rangle +\rangle$	$ x\rangle 0\rangle$	$ y\rangle -\rangle$	$ y\rangle +\rangle$	$ y\rangle 0\rangle$
$ x\rangle -\rangle$	0.	0.003	0.	0.006	0.
$ x\rangle +\rangle$		0.	0.003	0.	0.
$ x\rangle 0\rangle$			0.	0.	0.
$ y\rangle -\rangle$				0.	0.120
$ y\rangle +\rangle$					0.

Table III. Absolute squares of the spin mixing amplitudes $|\epsilon_{|i\rangle,|j\rangle}|^2$ for the setting of Fig. 2(c) in the main text. Only the $|y\rangle|0\rangle$ and $|y\rangle|-\rangle$ states mix significantly.

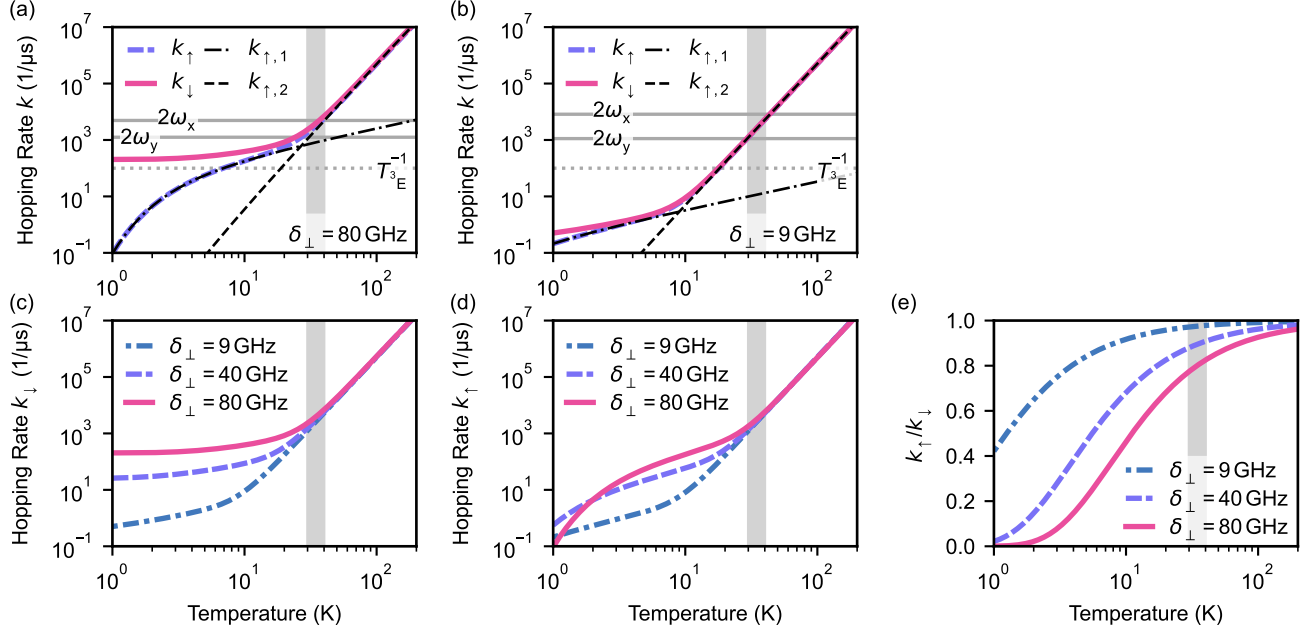


Figure S11. **Orbital hopping rates under different conditions** - (a) Rates up and down and contributions to the up rate of the one- and two-phonon processes for high strain. Also shown are the inverse optical lifetime T_{3E}^{-1} and twice the Larmor frequencies $2\omega_{x(y)}$ (in MHz) as horizontal lines. Unless specified otherwise, the same setting as in Fig. 2(c) and (d) of the main text is used in the entire figure. The 30 K – 40 K region where highest spin relaxation is observed is marked (gray shading). (b) Same for low strain. In both (a) and (b), the same overlap of the region of highest spin relaxation with the range where twice the Larmor frequencies and rates match is observed as explained for medium strain in the main text. (c) Effect of strain on the hopping rate down. (d) Effect of strain on the hopping rate up. (e) Ratio of rate up and down for different strains.

(for a given eigenstate)

$$\epsilon_{|i\rangle,|j\rangle} = \frac{\langle j|\tilde{e}s\rangle}{\langle i|\tilde{e}s\rangle}. \quad (\text{S15})$$

In Tab. III, we give the absolute squares of all relevant $\epsilon_{|i\rangle,|j\rangle}$, given the setting of Fig. 2(c).

VII. STRAIN DEPENDENCE OF ORBITAL HOPPING RATES

As the orbital hopping rates – paired with the spin mixing discussed in the main text – cause the observed spin relaxation process, we give a broader overview of their strain dependence here. The temperature dependence of the orbital hopping rates up (k_{\uparrow}) and down (k_{\downarrow}) are plotted in Fig. S11. We use the same parameter set as in Fig. 2(d) of the main text, but vary the in-plane strain δ_{\perp} . In Fig. S11(a), we present a similar setting as in Fig. 2(d), but for high strain $\delta_{\perp} = 80$ GHz. In Fig. S11(b) the same setting is also plotted for our low strain case of $\delta_{\perp} = 9$ GHz.

At high strain in Fig. S11(a), as discussed in the main text, two effects can be observed. First, at low temperature we find a significantly higher k_{\downarrow} for high strain δ_{\perp} (Fig. S11(c)). This is caused by the increase of the phonon mode density with energy. If the orbital branch splitting $\sim 2\delta_{\perp}$ is larger, a higher mode density is available for the

spontaneous one-phonon emission process (c.f. second term in Eq. 1 of the main text). Second, we also find a rapid increase of k_{\uparrow} at high strain with rising temperature (Fig. S11(d)). At very low temperature and high strain, the phonon modes required for the one-phonon absorption process are not populated. But with rising temperature, they rapidly get thermally activated and k_{\uparrow} reaches the high value of k_{\downarrow} . This can be seen in the detailed balance of the rates in Fig. S11(e), yielding a Boltzmann distribution of population. This combination of, first, a high k_{\downarrow} with, second, a rapidly increasing k_{\uparrow} below 10 K gives rise to the observed drop of spin contrast in Fig. 3(e) of the main text.
